EVALUATION OF CONE BEAM COMPUTED TOMOGRAPHY ENHANCEMENT USING A LIVER SPECIFIC CONTRAST AGENT FOR STEREOTACTIC BODY RADIATION THERAPY GUIDANCE

by

John David Lincoln

Submitted in partial fulfilment of the requirements
for the degree of Master of Science

at

Dalhousie University

Halifax, Nova Scotia

August 2018

Dedication

I dedicate this dissertation to the late Victor John Emmanuel Surajdeen. I strive every day to make you proud.

Table of Contents

List of Tables

List of Figures

Abstract

This study evaluated contrast enhancement provided by Gadoxetate Disodium, a liver specific contrast agent. Image quality from cone-beam computed tomography was benchmarked against helical fan-beam computed tomography for comparison in cylindrical and ellipsoidal geometries. Concentrations were diluted to 0.0125 – 0.1 mmol/kg corresponding to expected physiological concentrations in the liver. CBCT imaging parameters tube voltage, tube current, and filtration were investigated on board a TrueBeam STx linear accelerator. All parameters were optimized according to the contrast-noise ratio, following the Rose criterion. Acceptable combinations of contrast dose, tube voltage, tube exposure-time product, and filtration gave CNR greater than three. This was found in a range of expected concentrations from 0.025 to 0.1 mmol/kg for a tube voltage of 100 kV, half-fan bowtie filtration, and exposures between 2025 and 5085 mAs. This research provides optimized pre-clinical dosing information and imaging parameters to use Gadoxetate Disodium in a clinical trial with CBCT.

List of Abbreviations Used (in order of appearance)

WHO – World Health Organization

TARE – Trans-arterial Radio embolization

HCC – Hepatocellular Carcinoma

EBRT - External beam radiation therapy

LINAC – Medical Linear Accelerator

RF – Radiofrequency

EPID – Electronic Portal Imaging Device

TCP – Tumour Control Probability

NTCP – Normal Tissue Complication Probability

MLC – Multi-leaf Collimator

VMAT – Volumetric Modulated Arc Therapy

SBRT – Stereotactic Body Radiation Therapy

3D – Three-Dimensional

SRS – Stereotactic Radiosurgery

CNS – Central nervous system

SABR - Stereotactic Ablative Radiation Therapy

BED – Biological Equivalent Dose

LQ – Linear Quadratic

RILD – Radiation Induced Liver Disease

CT – Computed Tomography

2D – Two-Dimensional

DRR – Digitally Reconstructed Radiograph

CBCT – Cone-beam Computed Tomography

MRI – Magnetic Resonance Imaging

PET – Positron Emission Tomography

SNR – Signal-To-Noise Ratio

CNR – Contrast-To-Noise Ratio

Gd-EOB-DTPA – Gadolinium- Ethoxybenzyl- Diethylenetriaminepentaacetic Acid

GBCA – Gadolinium-Based Contrast Agent

FBCT – Fan beam Computed Tomography

HU - Hounsfield Units

EM – Electromagnetic

KERMA (Kerma) – Kinetic Energy Released in Matter

LET – Linear Energy Transfer

CSDA – Continuous Slowing Down Approximation

TFT – Thin Film Transistor

QDE – Quantum Detection Efficiency

SPR – Scatter-To-Primary Ratio

FOV – Field of View

SID – Source-To-Imager Distance

HFFA – Half-Fan Full Arc

FFHA – Full-Fan Half Arc

FFFA – Full-Fan Full Arc

XML – Extensible Markup Language

ASC – Analytic Spectrum Correction

SC – Scatter Correction

ROI – Region of Interest

NSF – Nephrogenic Systemic Fibrosis

DE – Dual Energy

EGSnrc – Electron Gamma Shower (National Research Council)

Acknowledgements

I would like to begin by thanking my supervisor Dr. James L. Robar for his support, guidance, and especially patience throughout these past two years. James, you are an incredible role model and if I can accomplish a fraction of what you have I will consider my career a success.

Next, I would like to thank my committee members: Dr. Sharon Clarke, Dr. Wladyslawa Cwajna, Dr. Alasdair Syme, and Dr. Chris Thomas. Thank you all for your continued support and the non-trivial task of having to read this dissertation.

I would be remiss if I did not acknowledge my peers. Dr. David Parsons, we both know that this work would not have been possible without you, and I have the utmost gratitude for your help these past two years. Cody, thank you for your friendship, late nights in the office, and early mornings at the gym. Michael, thank you for your friendship, and even later nights doing QA. Allan, Ethan, Lee, Parisa, Courtney, Conor, Lin, John and Christopher; thank you for answering questions whenever I had them. Liam, Carmen, Chris and Emma; thank you for keeping me sane. Bless up Jäg Committee.

Very special thanks go to Scott Purcell, Ian Porter, and Angela Henry. Thank you to support from Varian Medical Systems through Scott Purcell (again), Dr. Adam Wang, and Thanos Etmektzoglou. I would also like to thank staff at the NSHA: Dr. Krista Chytyk-Praznik, Dr. Mike Sattarivand, Dr. Mammo Yewondwossen, Dr. Thalat Monajemi, Dr. Amanda Cherpak, Dr. Robin Kelly, Dr. George Mawko, Dr. Steven Beyea, Elena Tonkopi, Jason Schella, Antoun Bou Laouz, Robert Moran, David Pepper, Darrel Discher, Corey Clements, Natasha McMaster, Clare Summers, Kathryn Moran, Rebecca Jessome, Carol Anne-Davis, Dr. Helmut Hollenhorst, and Dr. Liam Mulroy.

Lastly, my mom, dad, and sister. These past two years have been very trying. I am so lucky to have you three in my life, thank you for everything you have done, are doing, and will do, to help me along this crazy ride.

Chapter 1 Introduction

1.1 Preface

According to the Canadian Cancer Society's 2017 report **[1]**, one in two people will develop cancer at some point during their lifetime, while one in four are expected to die from cancer. These statistics are supported globally by the world health organization **[2]** (WHO) that cites one in six people worldwide will die from the disease. Of these numbers, colorectal cancers account for approximately 13% of all cases, while primary liver cancers account for 1.2% **[1]**. A study by Manfredi *et al.* from France concluded that the 14.5% of patients with colorectal cancer, also had synchronous liver metastases **[3].** Furthermore, Scorsetti *et al.* hypothesized that of all patients that have colorectal cancer, 30 – 70% will also develop liver metastases **[4]**.

Cancer is defined as a class of disease whereby rapid and/or abnormal cell proliferation occurs, which results in tumours **[5]**. Tumours are classified as benign where the disease does not have the capability to invade other normal tissues, or malignant, where the disease can spread, affecting surrounding tissues or organs. Malignant tumours are thus deemed cancerous, while benign tumours are not **[6]**.

Colorectal cancers are important when discussing liver disease as they are the most likely cancer to metastasize to the liver **[7]**. As they are the second most common cancer, this makes cancerous liver disease much more important. There exists a variety of treatment options for liver cancers such as chemotherapy, targeted therapy, surgery, ablation therapy, hormonal therapy and radiation therapy **[7]**.

Specific to radiation therapy, liver cancers may be treated with trans-arterial radioembolization (TARE), where a trans-catheter selectively delivers radioactive microspheres through the hepatic artery to primary liver disease such as hepatocellular carcinoma (HCC) **[8]**. Though effective in treating mid-stage disease in the liver, it is an invasive procedure by nature, requiring an interventional radiologist. This will introduce the complications associated with surgery.

External beam radiation therapy (EBRT) uses charged (electrons, protons) and uncharged (neutrons, photons) particles, to non-invasively treat cancer. These particles must have sufficient energy to reach disease in the body, and as such they must be accelerated to near-relativistic speeds **[4]**. The most common technology used to deliver radiation therapy is the clinical linear accelerator (LINAC), which accelerates electrons to these speeds. LINACs are a class of medical devices that accelerate a pencil beam of electrons, and then shape a treatment beam of electrons or photons to a prescribed target in the human body **[9**]. Briefly, a klystron is a component of some LINACs that amplifies the power of microwaves to create high power radiofrequency (RF) fields. An electron gun injects electrons into the system, where an energy transfer occurs from the RF field to the electrons. These electrons are then accelerated through a waveguide to reach energies on the order of mega-electron volts (MeV). These high energy electrons are then steered with a bending magnet normal to a desired treatment area. For photon treatments, the bending magnet sends photons directly incident on an x-ray target to produce a MV spectrum of photons. At this stage, photon production has occurred and can be made incident on a patient **[6]**. Figure 1.1 demonstrates an example of a modern LINAC from Varian Medical Systems that was used in this research:

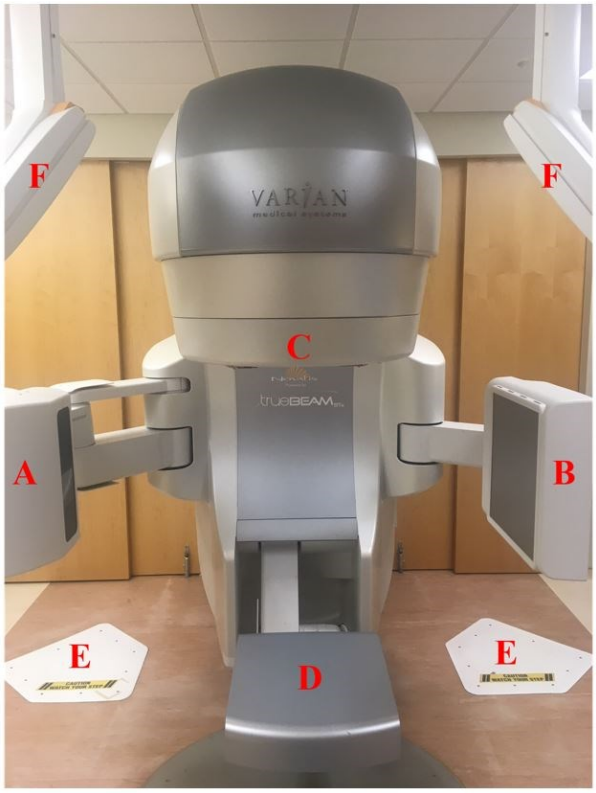

Figure 1.1: Medical LINAC at the Nova Scotia Health Authority. Model: Varian™ TrueBeam® STx (Varian Medical Systems Inc, Palo Alto, CA, USA). The legend denotes (A): the kilovoltage (kV) x-ray source, (B) the kV detector, (C) the collimator for megavoltage (MV) x-rays, (D) the electronic portal imaging device (EPID), (E) the ExacTrac® stereoscopic kV x-ray tube (BrainLab AG, Munich Germany), and (F) the ExacTrac® kV detector.

In the history of LINACs, technological advances have led to significant improvements in patient care. A clear example of this is the multi-leaf collimator (MLC). The MLC is comprised of two banks of grooved tungsten leaves that operate in tandem, each controlled by a motor switch **[10]**. Each of these MLC leaves can be controlled separately, thus complex apertures can be created to tailor the shape of the incident beam and to ensure minimal irradiation of normal tissue. Another example, and a more recent technology, is Volumetric Modulated Arc Therapy (VMAT) **[11]**, which leverages the ability of the gantry to rotate and modulate the MLC aperture to improve dose reduction to normal tissues. Although significantly reducing high dose volumes,

the compromise with VMAT is that it introduces a lower dose to a larger volume of tissue, compared to static beams. Nonetheless, this technique has facilitated significant dosimetric advantages in the context of stereotactic body radiation therapy (SBRT).

1.2 Stereotactic body radiation therapy

The word stereotactic is a two-part word of latin origins, with the first *stereo* coming from the *stereotaxy* ("three-dimensional (3D) arrangement") and the second *tact* ("touch") **[12]**. Derived from those origins, stereotactic has come to be defined in the medical literature as relying on a pre-defined 3D coordinate system to perform a medical intervention on targets inside (or outside) that physically touch the body **[12]**.

In radiotherapy the first stereotactic treatments were radiosurgery (SRS); defined by Lars Leksell as delivery of a high dose of radiation in a single treatment to disease in the brain **[13].** SRS harnessed the ablative effects of a single high dose treatment, compared to a fractionated treatment regime. Furthermore, SRS is used to treat very specific indications for the brain and central nervous system (CNS); venturing outside this anatomical region while delivering a small number of high dose fractions with high spatial accuracy is commonly known as stereotactic body radiation therapy, or stereotactic ablative radiation therapy (SABR). Fractionation in radiotherapy is defined as the daily dose of radiation obtained by subdividing the total prescribed dose into a specific number of treatments. Fractionation is thus a parameter used when calculating the biological equivalent dose (BED) to a tissue in question **[3]**.

$$BED = nd\left(1 + \frac{d}{\alpha/\beta}\right) \tag{1}$$

Where n is the number of fractions, d is the dose per fraction, and α/β is the alpha-beta ratio defined in the linear-quadratic (LQ) model for cell kill. This model is summarized in equation 2 below.

$$S = e^{-(\alpha D + \beta D^2)} \quad (2)$$

In this equation, S represents the total fraction of cells that survive a dose D of radiation, where α is the constant term that accounts for the linear part of the LQ model, while β is a constant that accounts for the quadratic part. The ratio of these parameters can then be used to describe the sensitivity of a specific tissue to fractionation.

Healthy liver is believed to have an α/β of 3 Gy, while HCC has an α/β of approximately 10 Gy **[14]**, where 1 Gy is defined as the unit of radiation dose equal to 1 Joule (J) of energy deposited per kilogram of medium. Plotting the cell survival curves with these values is given in figure 1.3 below:

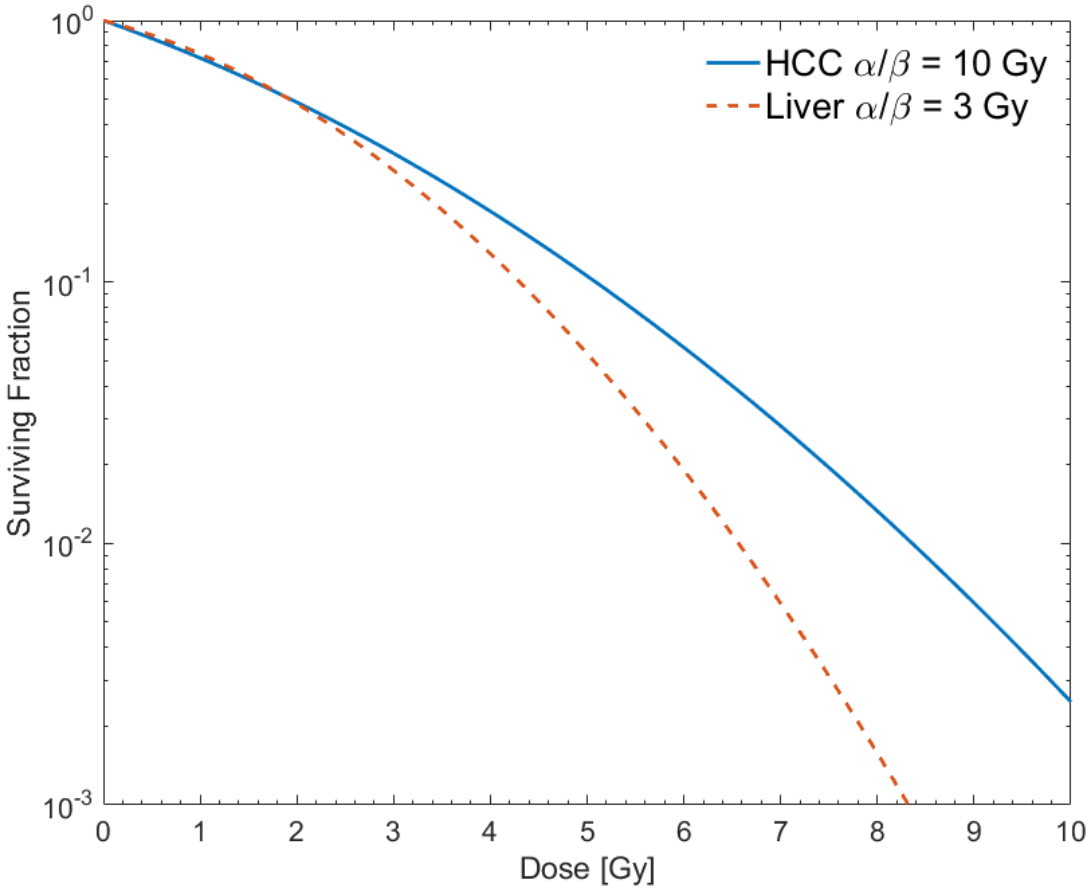

Figure 1.2: Plot illustrating the cell survival curve for HCC and healthy liver for a single fraction.

Figure 1.2 implies that decreasing the number of treatments (hypofractionating) may be favourable for treatment of liver disease and suggests a benefit of performing liver SBRT. Clinical trials have supported this notion **[4, 15, 16]**, and modern cancer centres routinely hypofractionate liver treatment. SBRT for the liver is typically performed in five 10 Gy fractions. Other fractionation schemes have investigated 14-30 Gy in a single fraction **[15, 16]**, while other common hypofractionation schemes range between 30-60 Gy in three fractions **[16]**. When hypofractionating, it is imperative to ensure that radiation is delivered accurately to the disease, while sparing the surrounding healthy anatomy.

The major consequence to consider when performing liver SBRT is the possibility of radiation induced liver disease (RILD). The liver is a critical organ serving many important functions in the human body, such as bile production, waste elimination, and protein synthesis. Following irradiation, the Child-Pugh scoring system is used to assess severity of liver disease **[17]** in terms of a comparison with laboratory parameters before radiotherapy. RILD effects can arise two weeks to four months after irradiation and can result in liver failure or death **[17]**. RILD risk is directly proportional to the mean radiation dose delivered to healthy liver tissue, implying that there is a dose-volume effect **[17]**. The effective volume (V_{eff}) is defined as the normal liver volume that if irradiated to the prescribed dose, would be associated with the same NTCP as the non-uniform dose delivered. In some cases, if V_{eff} is kept low, liver tolerance to radiation is seen up to 90 Gy **[17]**. Nonetheless, established toxicity parameters state that mean liver dose associated with a 5% risk of classic RILD is 28 and 32 Gy for primary liver disease and metastases respectively. To preserve adequate liver function, the minimum volume that must be spared during radiotherapy is 700 cc, where the maximum dose allowed is 15 Gy over 3 fractions **[17]**.

1.3 Image guidance for SBRT

Image guidance is defined as the matching procedure between the image that is used to plan a patient's radiotherapy treatment, and images that are acquired at the time of treatment. Precise image guidance is required for SBRT treatments due to strict matching conditions to ensure accurate radiation delivery. Radiation treatment plans require electron density information to accurately model interaction of ionizing radiation with tissues in the body. Electron density will be defined using the following equation from **[18]**:

$$N_e = \frac{N_A Z_{eff}}{(A/n_i)} \tag{3}$$

where N_A is the constant Avogadro's number, Z_{eff} is the effective atomic number a material specific parameter, A is the molecular weight, and n_i is the total number of atoms in the compound.

To determine this information, a computed tomography (CT) dataset is first acquired. At the time of treatment to match the patient's anatomical geometry to the planning CT, as illustrated in figure 1.1 modern LINACs have on-board imaging with both MV and kV potentials. Image guidance matching is typically performed using the LINAC's kV imaging system owing to the reduced dose and improved image quality **[19]**. Once the patient is roughly aligned to the mechanical isocenter using lasers, there are multiple options for image guidance. Two-dimensional (2D) orthogonal projections can be acquired to match with a pre-calculated digitally reconstructed radiograph (DRR) using Siddons method **[20]**. Furthermore, a volumetric image can be reconstructed to match with the 3D image-set that was used for planning. Considering the components from figure 1.1, a cone-beam CT (CBCT) requires an x-ray source incident on a flat panel detector. A cone of x-rays is made incident through an object onto the detector, and for every gantry angle a different projection is acquired. The volume is then reconstructed using the filtered backprojection algorithm of Feldkamp, Davis, and Kress **[21]**. Given the volumetric data acquired at the time of treatment, matching is performed by the radiation therapists by co-registration to the planning CT. Sufficient matching is taken as a function of distance from the expected location in units of millimeters for SBRT, where the treatment plan will have a specific matching condition that permits the treatment. If the condition is not met, the patient must be repositioned, and the image guidance procedure repeated, also known as set up imaging.

It is especially important in high dose stereotactic treatments to have highly accurate image guidance to avoid permanent radiation damage to healthy tissues, and to ensure local tumour control. Typical matching conditions for liver SBRT are less than 3 mm difference between planning CT and CBCT, in accordance with the treatment margins combined with the overall system accuracy **[22]**. However, there are specific anatomical considerations when performing image guidance for the liver. Primary and metastatic tumours are not easily visualized in the liver because their soft-tissue compositions are similar to the normal liver tissue surrounding them **[23]**. Examples of this disadvantage are supported by various clinical trials with liver SBRT that required magnetic resonance imaging (MRI) and positron emission tomography (PET) to supplement the planning process for image guidance **[4, 15, 16]**. In CBCT, bony anatomy does not serve as a reliable surrogate for liver, and thus matches are made with the liver itself **[4]**. A significant drawback to this approach is that the liver is a deformable organ that is also susceptible to respiratory motion. For these reasons, when deciding whether to treat a patient with liver disease using radiation, the prescribing oncologist must weigh the risk of increasing treatment margins, and thus more healthy tissue irradiation, against the benefit of tumour eradication.

Since the tumour is often not conspicuous within the liver volume in CBCT, image guidance often involves implantation of metal (gold) fiducial markers inside or near the tumour. This current "gold standard" of practice has been studied extensively **[24, 25, 26]**. Furthermore, according to a study performed by Seppenwoolde *et al.* **[27]** liver SBRT treatment precision is dependent on the implanted marker to tumour distance. It is thus evident that using tumour surrogates will still have limited precision. Moreover, accuracy of image guidance is improved with greater numbers of fiducial markers surrounding a primary liver cancer **[27]**. It becomes

more difficult to implement fiducial markers for multiple metastases cases, in which numerous injection sites of fiducials may be required **[24].** Oldrini *et al.* evaluated the feasibility of implanting fiducial markers in the liver, citing the factors an interventional radiologist must consider in the procedure **[25]**. This study quoted risk of hemorrhage in patients that have coagulation disorders when trying to ensure a small margin between fiducial markers. To mitigate this risk, only 2-3 fiducial markers were placed around the tumour **[25]**. In addition, liver deformation was quoted as a limiting factor in the accuracy of marker positioning, which in turn decreased accuracy in image guidance. When considering the cost for implanting fiducial markers as a method to improve image guidance, there are several major factors. First, the cost of fiducial markers can range between 100 to 200 USD per patient **[28]**. The cost of the interventional radiologist must also be considered for this procedure, in addition to the cost of anesthesia, an anesthesiologist, nursing personnel, and equipment **[29]**.

The possible complications and significant cost demonstrate a need for a non-invasive method to improve the image guidance accuracy for liver SBRT. This need was addressed by Jones *et al.* in 2013 **[30]** and later by Eccles *et al.* in 2016 **[31]**. These studies explored the use of the diagnostic CT iodinated contrast agents Isovue-370 and Visipaque, respectively, used in for CBCT image guidance. Although qualitative image enhancement was found, quantitatively Jones *et al.* never found a signal-to-noise ratio (SNR) > 3, while Eccles *et al.* concluded average tumour enhancement and hepatic vascular enhancement contrast-to-noise ratio (CNR) = 4.85 and 1.75, respectively. Both concluded that the use of iodinated contrast was not feasible for liver SBRT treatments where multiple CBCT acquisitions may be required. This is owing to the fact that the human body's time course for iodine-based contrast agents last on the order of minutes. When compared to a single CBCT acquisition with the maximum gantry velocity of 6º per

second over a full 360º arc, the time limitation is one minute. Hence, although non-invasive, the iodinated contrast method was shown to have limited clinical utility in the context of image guidance compared to implantation of markers into the liver.

1.4 Gadoxetate Disodium

Gadoxetate disodium, short for gadolinium-ethoxybenzyl-diethylenetriaminepentaacetic acid (Gd-EOB-DTPA), is a gadolinium-based contrast agent (GBCA) that was introduced by Schuhmann-Giampieri *et al.* **[32]** in 1992 for use in T1-weighted MRI. The molecule is a combination of the lipophilic EOB moiety with a Gd-DTPA salt via covalent bonding to provide improved hepatocellular specificity, as compared to Gd-DTPA alone. Moreover, there was a need for a contrast agent that would last in the liver with washout times on the order of 1-2 hours, compatible with the times required for diagnostic MRI acquisition protocols. The Gd^{3+} ion is ideal for MRI because of its paramagnetic nature; however, Gd is also known to enhance x-ray imaging techniques because of its high atomic number.

The contrast agent is currently marketed as Primovist® (Bayer AG, Leverkusen, Germany) in Canada and Europe, and as Eovist® in the United States. The Primovist® product monograph **[33]** states that the contrast agent is indicated for use with T1-weighted MRI of the liver for diagnostic purposes. The elimination of the contrast agent follows a biphasic mode of action, which means that it is eliminated from the body via two main pathways. These two pathways are the renal and hepatobiliary, owing to the agent's hepatocellular specificity. The mean terminal elimination half-life is approximately one hour **[33]**. The recommended dose for patient administration is 0.025 mmol/kg. It is quoted in mmol per kilogram of body-weight (kg BW), as mass is known to influence the pharmacokinetics of the contrast agent **[33]**. Where not explicitly

stated in this thesis, all reference to the unit mmol/kg will refer to "per kilogram of body weight".

The first pre-clinical tests to understand the pharmacokinetic properties of the contrast agent were performed by Schuhmann-Giampieri *et al.* **[32]**, in animal models, including mice, rats, and cynomolgus monkeys. This work further examined T1 signal enhancement, and in-vitro binding to human liver plasma cells. The authors concluded that the contrast agent exhibited significant hepatic uptake with high T1 relaxivity allowing for delineation of small tumours in the liver. Furthermore, they were able to determine, based on the dose administered and pharmacokinetic behavior, the appropriate timing to achieve optimal enhancement.

While clinical trials were beginning with Gadoxetate Disodium and MRI **[34, 35, 36, 37]**, Schmitz *et al.* **[38, 39]** performed pre-clinical and a phase IIA clinical trial with Gadoxetate Disodium and helical fan-beam CT (FBCT). The pre-clinical study investigated CT attenuation with iodinated contrast enhancement to the attenuation achieved using Gadoxetate Disodium **[33]**. The work also examined two animal models, dogs and rabbits, in terms of qualitative and quantitative CT enhancement. The authors concluded a linear relationship between CT attenuation, as measured in Hounsfield units (HU), and concentration of both iodinated and gadolinium-based contrast agent. Furthermore, the animal studies concluded that there was effective uptake of the contrast agent in the liver, providing sufficient results to justify the clinical trial in humans. The phase IIA clinical trial examined 15 patients with suspected or known liver malignancies, that underwent Gadoxetate Disodium enhanced CT at doses of 0.2, 0.35, and 0.5 mmol/kg. These doses correspond to 8, 12, and 20 times the dose that is recommended for MRI enhancement with Primovist®. Enhancement was observed relative to a pre-contrast CT at 80 and 150 minutes post injection. The trial concluded acceptable image

quality and patient tolerance to justify continued scientific study given a similar target population.

1.5 Research Objectives

The previous sections have provided the essential background and motivation for the research presented in this dissertation. To summarize:

1) SBRT is a promising technique that may be used to deliver ablative radiation dose in the treatment of primary and metastatic liver cancer.
2) CBCT imaging may be used in the guidance of liver SBRT, however due to the poor visualization of the tumour relative to surrounding normal liver, the approach often involves invasive insertion of metallic fiducial markers.
3) CBCT can be enhanced with an intravenous contrast injection of iodine **[30**, **31]**, but the time-course for washout is not compatible with the duration of CBCT image data and adjustment to patient position.
4) A readily available liver specific contrast agent (Gd-EOB-DTPA) exists, but it is only marketed for use with MRI.

To our knowledge, there has not been a systematic quantification of CNR in Gadoxetate Disodium enhanced FBCT or CBCT images. This work aims to provide a quantitative analysis of the necessary FBCT and CBCT parameters if Gadoxetate Disodium is to be used in a radiotherapy setting. The work that formed this dissertation is comprised of a series of experiments that aim to determine:

1) The achievable contrast-to-noise ratio for Gadoxetate Disodium enhanced helical FBCT, with comparison to results found by Schmitz *et al.* **[38, 39].**

2) The achievable CNR for Gadoxetate Disodium enhanced CBCT, and image acquisition parameters that maximize this aspect of image quality.

The experiments for (1) and (2), above, are repeated using phantoms that are "ideal" with regard to geometry and "realistic", i.e., representing the geometry of the abdomen.

The following chapters build on the concepts discussed in the introductory chapter with a focus on the underlying physical concepts. The second chapter discusses the physics of radiation transport, while the third chapter presents relevant medical imaging theory. The fourth chapter gives the methodology for all experiments and analysis to ensure repeatability. The fifth and sixth chapters present the results and discussion respectively, while the final chapter concludes the dissertation and suggests possible future work.

Chapter 2 Radiological Physics theory

This chapter contains a discussion of the physical theories behind radiation transport that dictate how radiation interacts with the human body. First, an important distinction is made between ionizing and non-ionizing radiation. The chapter then discusses photon interactions with matter. These concepts are then combined for a brief discussion on how the theory relates to the proposed research.

2.1 Ionizing Radiation

Radiation can be roughly divided into two groups: ionizing and non-ionizing. Ionizing radiation is defined as radiation with sufficient energy to cause an outer-shell (valence) electron to leave an atom **[40]**. Conversely, non-ionizing radiation is defined as all other radiation with insufficient energy to permit escape of an atom's valence electron. The law of energy conservation dictates that radiation must possess kinetic or quantum energy to be considered ionizing **[40]**. For the intent of this dissertation, all discussion regarding radiation, unless otherwise stated, is considered ionizing radiation. For a more comprehensive discussion on non-ionizing radiation, the reader is referred to **[41, 42]**.

There are various types of radiation to be considered. The first to be discussed is gamma (γ) rays, which are defined as electromagnetic (EM) radiation that may be emitted from the nucleus of an atom or produced from an annihilation event between matter and matter. A straight forward example of annihilation is that of an electron (β^-) physically colliding with a positron (β^+), yielding two annihilation photons **[40]**. The equation that describes the quantum energy of any electromagnetic photon is given as:

$$E_\gamma = h\nu = \frac{hc}{\lambda} \quad (4)$$

Where h is Planck's constant equal to 6.626 x 10^{-34} J s, ν is the frequency also described by the quantity c/λ, where c is a constant (speed of light in a vacuum) equal to 2.998 x 10^8 m/s and λ is the wavelength of EM radiation **[40]**.

X-Rays are a result of charged particles emitting EM radiation due to changing atomic energy levels or slowing down due to Coulombic interactions. The potential difference used to accelerate charged particles that emit x-rays is used to classify their types. A list can be found in **[40]** however for this dissertation, the focus is predominantly on "diagnostic-range x-rays" (20-120 kV), with a brief discussion on "megavoltage x-rays" (> 1 MV).

Although γ and x-rays are uncharged and massless, radiation can also be in the form of charged massive particles. The combination of electrons, protons, neutrons, and heavy ions make up a subset of radiation called "directly ionizing radiation", whose energy is deposited directly to matter through Coulombic interactions. This differs from "indirectly ionizing radiation" where γ and x-rays must first transfer their energy to charged particles to permit direct energy deposition **[40]**.

Quantities relevant to transfer and absorption of energy from ionizing radiation are **[40]**:

1. Kerma (K).
2. Absorbed dose (D).
3. Exposure (X).

Kerma (kinetic energy released in matter) is defined in terms of ε_{tr} the energy transferred, and ε_{tr}^{n}, the net energy transferred to charged particles by indirectly ionizing radiation. It can be

further classified based on whether energy is transferred nearby through excitation and ionization (collision Kerma K_c) or is carried away by photons (radiative Kerma K_r).

$$K = K_c + K_r \tag{5}$$

K has units of J/kg which are commonly referred to as 1 *gray* (Gy) equal to 1 J/kg.

Given a spectrum of photon energies, K can be obtained by summing over all energies in the spectrum:

$$K = \int_{E_0}^{E_{Max}} \Psi'(E) * \left(\frac{\mu_{tr}}{\rho}\right)_{E,Z} dE \tag{6}$$

where the energy fluence is denoted by $\Psi'(E)$ and $\left(\frac{\mu_{tr}}{\rho}\right)_{E,Z}$ is a term called the *mass transfer coefficient* **[40]**. In the same way, K_c is defined as a function of $\left(\frac{\mu_{en}}{\rho}\right)_{E,Z}$, the *mass absorption coefficient*. When both coefficients are summed, they form the *mass attenuation coefficient* that dictates how many photons will interact with the material in question. This term is discussed further below **[40]**.

Absorbed dose, D, is a quantity that describes energy absorbed by matter by any type of radiation but delivered by charged particles. It is defined mathematically as:

$$D = \frac{d\epsilon}{dm} \tag{7}$$

where ϵ is the average energy imparted to the medium in question **[40]**.

Exposure, X, is a quantity defined by the ratio:

$$X = \frac{dQ}{dm} \tag{8}$$

where dQ is defined as the absolute total charge of single sign ions produced in air when all electrons released by photons in a mass of air dm are stopped completely. This quantity is useful as it is proportional to energy fluence of a photon spectrum, furthermore an x-ray field can be characterized at a point as a function of X regardless of if there is air at that point **[40]**.

2.2 Photon interactions with matter

As discussed by Attix **[40]** there are four main interactions that must be considered for photons, whether they be γ or x-rays. These interactions are:

1. Rayleigh (coherent) scattering.
2. Photoelectric effect.
3. Compton (incoherent) scattering.
4. Pair production.

Each will be explained briefly, with a more thorough explanation of those relevant to x-ray radiography (photoelectric effect and Compton scattering) **[40]**.

2.2.1 Rayleigh scattering

Also known as coherent scattering, Rayleigh scattering occurs when a photon is scattered elastically by the action of an entire atom. This results in minimal to no loss in energy of the photon, while the atom will recoil sufficiently to preserve conservation of momentum. The negligible energy loss leads to the notion that this interaction will not provide a contribution to dose and will not cause ionization or excitation **[40]**. The atomic cross section for Rayleigh scattering events is proportional to:

$$ {}_a\sigma_R \approx \frac{Z^2}{(h\nu)^2} \tag{9} $$

Where ${}_a\sigma_R$ denotes the atomic cross section, Z denotes the atomic number of the atom in question, and $h\nu$ is the energy as given in equation 4. The atomic cross section is measured in cm^2/atom; however, it is also useful to express the quantity in terms of its density (mass units):

$$ \frac{\sigma_R}{\rho} \approx \frac{Z}{(h\nu)^2} \tag{10} $$

where ρ is the density of Z atoms giving mass attenuation units of cm^2/g **[40]**.

It is important to note that the relations in equations 9 and 10 are proportionalities instead of exact equations. They indicate that the probability of Rayleigh scattering is directly proportional to the atomic number and the inverse square of the photon's energy.

2.2.2 Photoelectric Effect

The photoelectric effect occurs when an incident photon with kinetic energy given by equation 4 interacts with a tightly bound atomic electron, typically in one of the inner shells of a high Z atom. The potential energy binding the electron to the atomic shell is called the binding energy and denoted by E_b. Therefore, to overcome E_b the photon energy must be greater than the binding energy. If this condition is met, the photon is completely absorbed, with an ejected *photoelectron* receiving all the remaining kinetic energy **[40]**. This relation is given in equation 11:

$$ KE = h\nu - E_b \tag{11} $$

where KE is the remaining kinetic energy of the photoelectron.

A more comprehensive illustration of the kinematics of the photoelectric effect is given in figure 2.1:

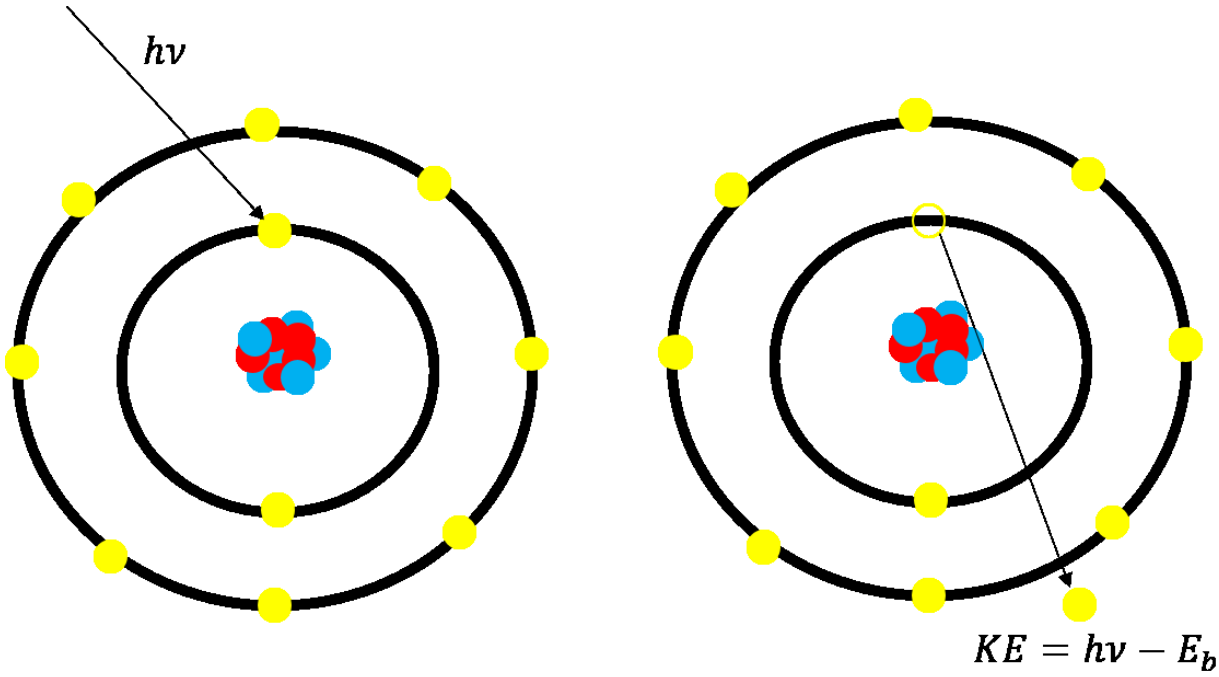

Figure 2.1: Illustration of the kinematics of the photoelectric effect

When considering photon interactions in the diagnostic energy range, the photoelectric effect is extremely important **[40]**. This is reflected in the dependence of the photoelectric interaction cross section on energy, given in equation 12:

$$_a\tau = k\left(\frac{Z^n}{(h\nu)^m}\right) \tag{12}$$

where k is a constant that incorporates constants that arise when integrating over all possible angles of photoelectron emission, Z is the atomic number, and $h\nu$ is the energy of the incident photon **[40]**. Like equation 5, this relation gives units of cm^2/atom. According to **[40]** n is equal to 4 for $h\nu$ =100 keV, and approximately 4.6 at 3 MeV. Furthermore, m is equal to 3 for $h\nu$ =100

keV, and approximately 1 at 5 MeV. Below 100 keV, *n* and *m* are approximately equal 3 and 4 respectively, giving the photoelectric mass attenuation coefficient formalism of equation 13:

$$\frac{\tau}{\rho} \approx \left(\frac{Z}{h\nu}\right)^3 \tag{13}$$

where ρ is the density of *Z* atoms giving mass cross section units of cm^2/g **[40]**.

Although the energy transfer in the photoelectric effect has been briefly discussed, an explanation is needed for what happens after the photoelectron absorbs the initial photon. When an electron is removed from an inner atomic shell (photoelectric effect), the vacancy is filled by electrons transitioning from an outer shell. These transitions can produce photons in a process called *fluorescence* or electrons through the *Auger effect* **[40**]. This concept is more easily described with a schematic as illustrated in figure 2.2:

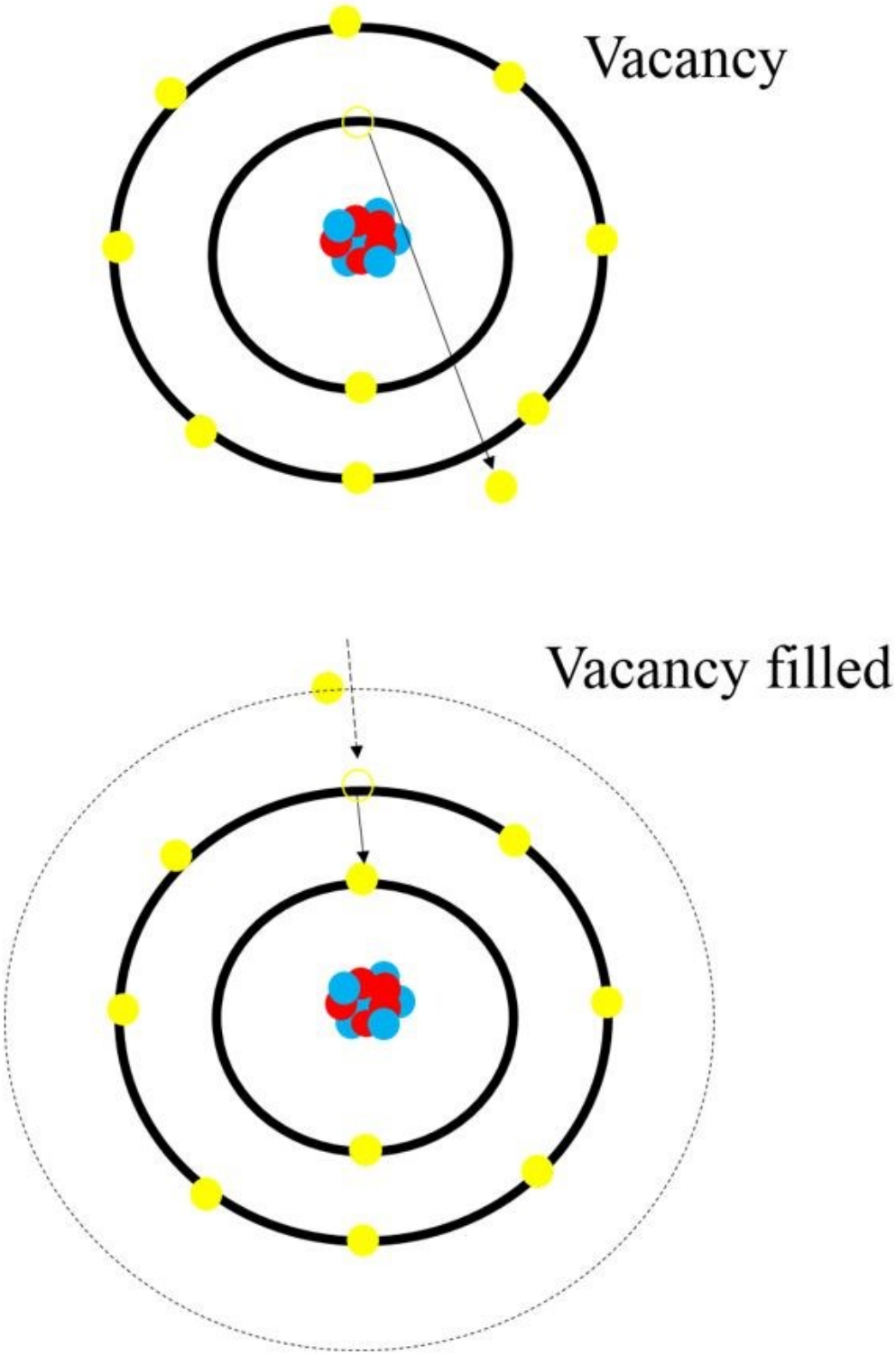

Figure 2.2: Illustrating the kinematics of an empty vacancy being filled to permit either fluorescence or the auger effect.

A transition to K- or L-shell vacancy may cause a fluorescent x-ray to be emitted with quantum energy given by equation 4, equal to the transition's energy level difference, where the probability of occurrence is given by *Y* **[40]**. The mass energy transfer coefficient for photoelectric absorption is given by:

$$\frac{\tau_{tr}}{\rho} = \frac{\tau}{\rho}\left[\frac{h\nu - P_k Y_k h\bar{\nu}_k - (1 - P_k)P_L Y_L h\bar{\nu}_L}{h\nu}\right] \tag{14}$$

where $P_{K,L}$ account for the fraction of interactions occurring in the *K* or *L* shell respectively, $h\nu$ is the energy of the incident photons, and $h\bar{\nu}_{k,L}$ correspond to average fluorescent x-ray energies in transitions to *K* and *L* shell respectively **[40]**.

Transitions from outer-shells will in turn create more vacancies that will need to be filled. The *Auger effect* describes the process by which an electron "cascade" may occur to continually fill these vacancies. The *Auger effect* permits another pathway for the propagation of kinetic energy if it is insufficient to overcome the binding energy of a specific electron shell.

2.2.3 Compton scattering

Rayleigh scatter was defined as coherent scattering due to the action of the incident photon with an entire atom. Compton scatter, also known as incoherent scattering, occurs when a free (negligible binding energy) electron interacts with by an incoming photon, yielding a photon of lesser energy due to the interaction, as well as a recoil electron **[40]**. The kinematics of a Compton scattering event are illustrated in figure 2.3:

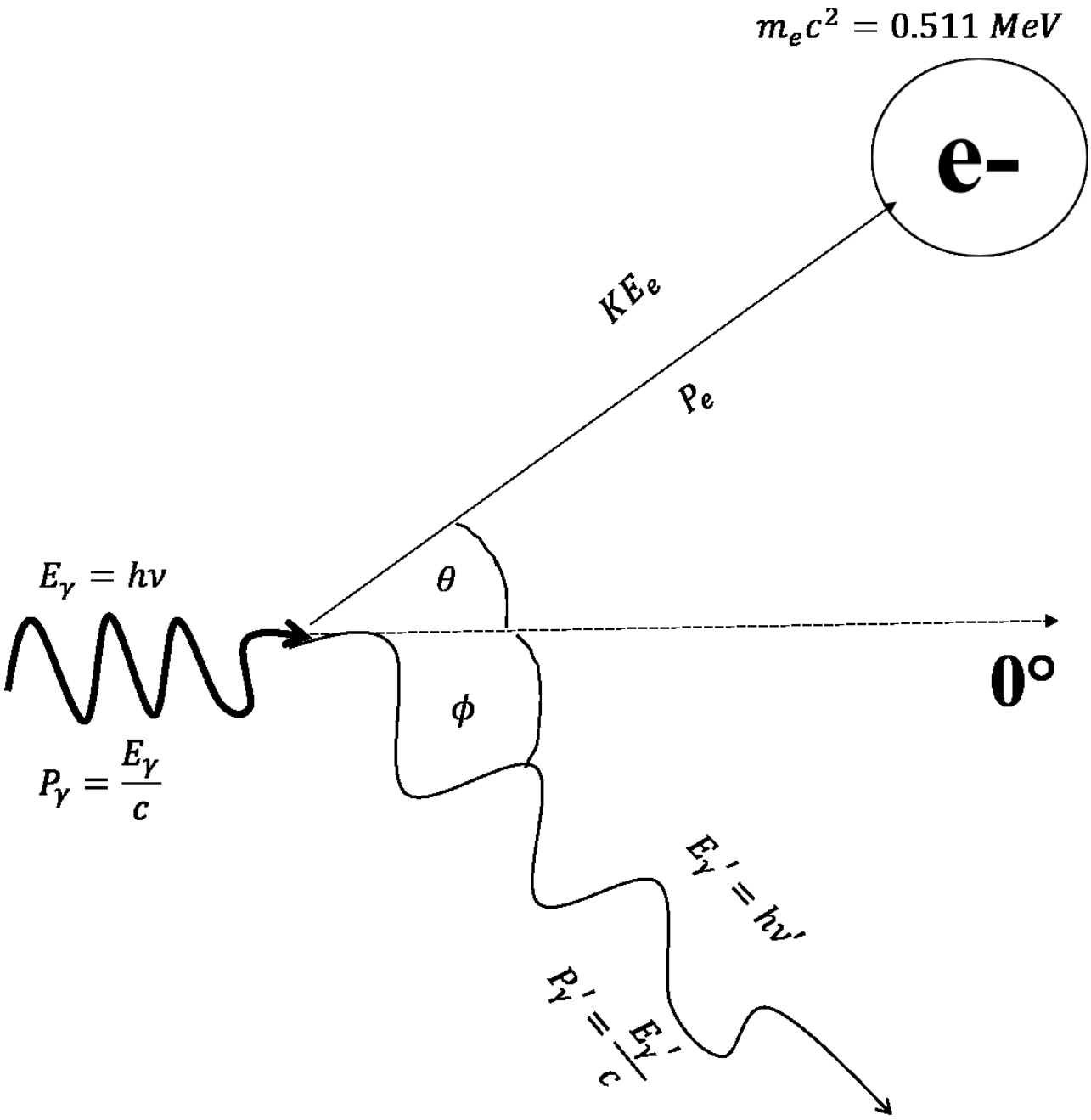

Figure 2.3: Illustrating the kinematics of a Compton scattering event, where a photon physically collides with an electron, resulting in a scattered photon and recoiling electron with directions given above. The rest mass energy of the electron is given as 0.511 MeV.

Such an event can be further described using the relativistic forms of conservation laws for energy and momentum, yielding the three main equations that describe Compton kinematics **[40]**:

$$KE = h\nu - h\nu' \tag{15}$$

$$h\nu' = \frac{h\nu}{1 + \left(\frac{h\nu}{m_e c^2}\right)(1 - \cos\phi)} \tag{16}$$

$$\cot\theta = \left(1 + \frac{h\nu}{m_e c^2}\right)\tan\left(\frac{\phi}{2}\right) \tag{17}$$

The equations predicted by Compton theory account for the fact that high energy incident photons will result in smaller electron deflections as compared to low energy predictions made by Thomson **[40]**. Although Thomson's theory failed to correctly characterize photon scattering at high energies, Klein and Nishina (K-N) were able to rewrite Thomson's formula for the differential cross section in a form that did not assume the scattered and incident photons had the same energy. This is given in equation 18 **[40]**:

$$\frac{d_e\sigma}{d\Omega_\phi} = \frac{r_0^2}{2}\left(\frac{h\nu'}{h\nu}\right)\left(\frac{h\nu}{h\nu'} + \frac{h\nu'}{h\nu} - \sin^2\phi\right) \tag{18}$$

with units of cm^2 per electron per solid angle as measured in steradians (Ω). In this formalism, r_0 is the constant classical electron radius. When integrated over all photon scattering angles, an analytic solution was found, and given as the total K-N cross section per electron:

$${}_e\sigma = 2\pi r_0^2\left\{\frac{1+\epsilon}{\epsilon^2}\left[\frac{2(1+\epsilon)}{1+2\epsilon} - \frac{\ln(1+2\epsilon)}{\epsilon}\right] + \frac{\ln(1+2\epsilon)}{2\epsilon} - \frac{(1+3\epsilon)}{(1+2\epsilon)^2}\right\} \tag{19}$$

where a readability substitution was made for ϵ to denote $\frac{h\nu}{m_0 c^2}$. Perhaps the most important takeaway from equation 18 is the lack of dependence on atomic number of the K-N cross section **[40]**. Therefore, the K-N cross section in cm^2/atom is simply:

$$_a\sigma = Z\ _e\sigma \tag{20}$$

The mass attenuation coefficient is then expressed in cm^2/g as:

$$\frac{\sigma}{\rho} = \frac{N_A Z}{A}\ _e\sigma \tag{21}$$

where N_A is Avogadro's constant measured in mol^{-1}, and A is the atomic weight measured in units of g/mol **[40]**. Given that the ratio between Z and A is approximately constant, equation 21 implies that the Compton mass attenuation coefficient is independent of atomic number **[40]**.

2.2.4 Pair production

Pair production occurs when a photon interacts with a Coulomb force field near an atom's nucleus, giving rise to matter and anti-matter in the form of an electron and positron **[40]**. "Triplet production" is a similar phenomenon when occurring in the field of an atomic electron, where two electrons and a positron result. The incident photons must possess a minimum quantum energy of $2m_0c^2$ for pair production and $4m_0c^2$ for triplet production **[40]**. This is because at minimum, to create two particles of equal electron rest mass (m_0c^2 = 0.511 MeV), energy conservation dictates that the energy before pair production must have been greater than two times the rest mass **[40]**. In the case of triplet production, even though the total energy being converted to mass is $2m_0c^2$, conservation of momentum dictates that the original photon must have been moving at 80% the speed of light, and thus have minimum energy of $4m_0c^2$ **[40].**

Considering that this minimum photon energy is much greater than the diagnostic x-ray range, it is a safe assumption to not consider pair production interactions for imaging.

For completeness, the atomic cross section for pair production is given based on work done by Bethe and Heitler as:

$$_a\kappa = \sigma_0 Z^2 \bar{P} \tag{22}$$

where σ_0 is a constant fraction of the classical electron radius, and $\bar{P}$ is a function of the incident photon energy and atomic number **[40]**. This allows us to rewrite equation 22 in the form of mass attenuation coefficient:

$$\frac{\kappa}{\rho} = \frac{N_A}{A}\ _a\kappa = \frac{N_A}{A}\sigma_0 Z^2 \bar{P} \tag{23}$$

2.2.5 Mass attenuation coefficient

The sections above have discussed the physical theories behind photon interactions with matter in terms of the kinematics of interactions and probabilities of interaction through cross sections. For every material, these mass attenuation coefficients can be summed to form the total probability of interaction per unit density or the total mass attenuation coefficient:

$$\frac{\mu}{\rho} = \frac{\sigma_R + \tau + \sigma + \kappa}{\rho} \tag{24}$$

It is clear from equation 24 that the total mass attenuation coefficient $\frac{\mu}{\rho}$ is a cumulative probability from each contributing interaction.

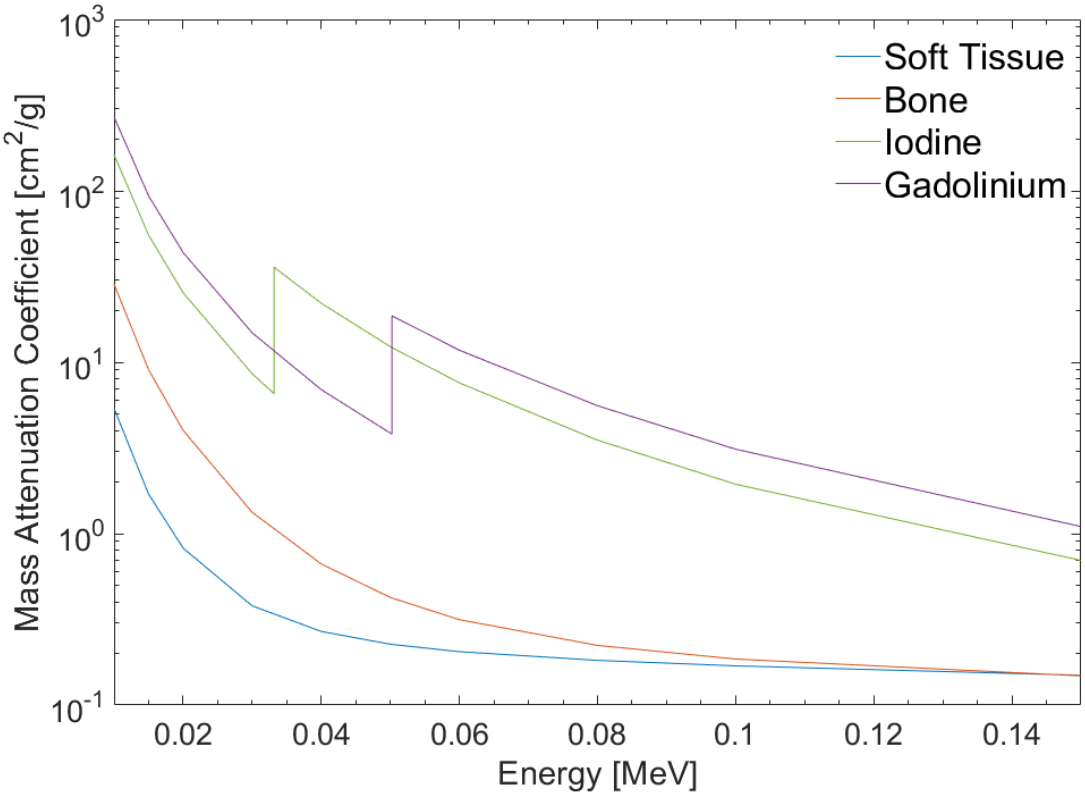

Figure 2.4: Illustrating the mass attenuation coefficient as a function of energy for ICRU44 Soft Tissue **[43]**, ICRU44 bone, iodine, and gadolinium, taken from NIST **[44]**.

ICRU44 Soft Tissue was deemed appropriate in terms of illustrating the differences in attenuation between liver and a GBCA. Figure 2.4 summarizes the theory that a GBCA should exhibit differential attenuation compared to tissue in the diagnostic energy range is confirmed.

2.3 Contributions to medical images

When considering the contributions to medical images it is important to note that this research focused on x-ray imaging in the diagnostic x-ray range (20-120 keV). As discussed previously, the predominant photon interaction in this energy range is the photoelectric effect due to the inversely cubic proportionality between the interaction cross section with energy **[40]**. It is exacerbated in materials that have high atomic numbers because of the additional cubic

dependence on Z. Imaging Gadoxetate Disodium, a contrast agent whose primary gadolinium molecule has a high atomic number (Z=64) should thus provide significant attenuation as demonstrated in figure 2.5:

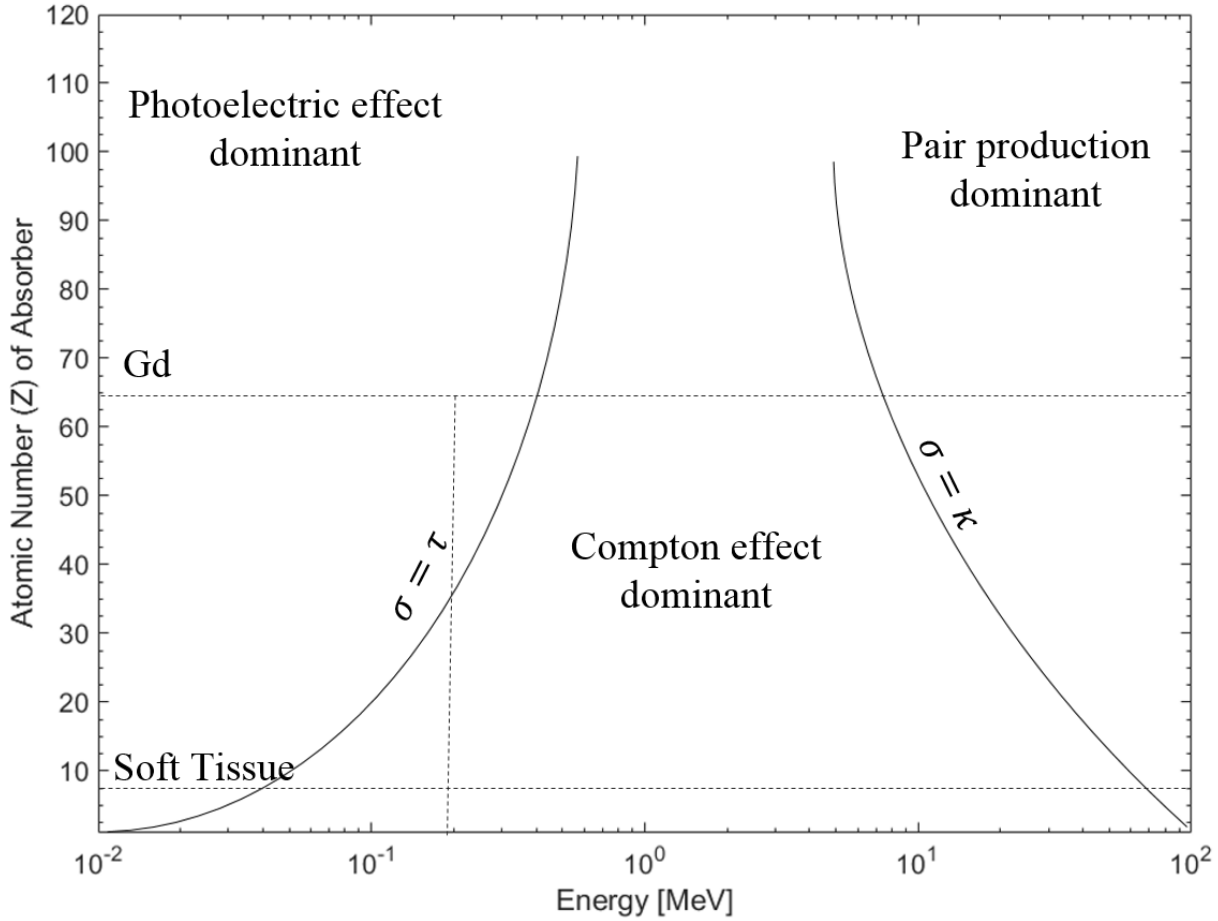

Figure 2.5: Plot of atomic number (Z) as a function of energy to demonstrate equi-probability of interactions.

In many cases, tissue may be approximated by water whose effective atomic number is approximately 7.42 **[40]**. When comparing this to Z=64 for gadolinium, in the diagnostic energy range, there should be a significant difference in attenuation between the two materials.

Chapter 3 Medical imaging theory

This chapter contains a discussion on the theories behind medical imaging including planar and volumetric imaging x-ray imaging. The mathematical theories behind volumetric reconstruction will be discussed, as well as those for CBCT calibrations. Metrics of quality will be reviewed, as well as artifacts that contribute to the degradation of image quality.

3.1 Planar X-ray imaging

As illustrated in the schematic of figure 3.1, x-rays are generated by accelerating electrons towards a target material. These electrons undergo interactions with the target producing a spectrum of x-ray photons that are used in medicine for diagnostic and/or treatment purposes. The electrons are released by thermionic emission in which a cathode filament is heated with a specific current which in turn dictates the tube current (mA) and temperature. Once released, the electrons experience the tube potential between cathode and anode. The maximum peak-to-peak tube potential characterizes each x-ray spectrum and is denoted by *kVp*.

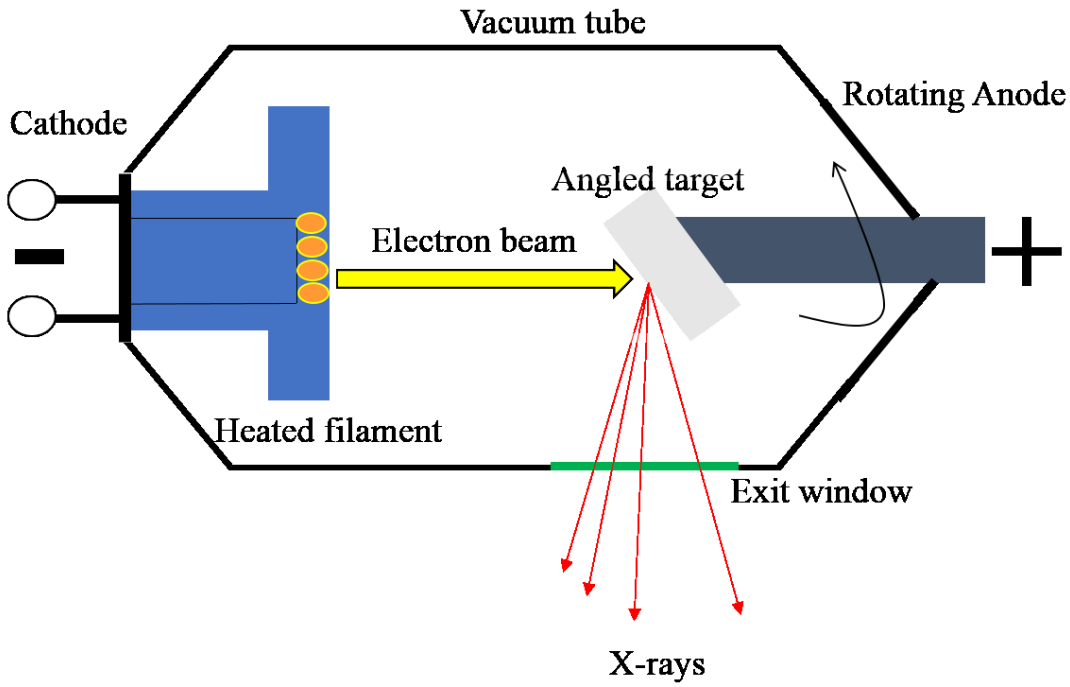

Figure 3.1: Illustrating a schematic for a generic x-ray tube with relevant components as found in **[47]**.

X-ray spectra are significantly influenced by changes in x-ray tube parameters. For example, x-ray tube output is known to depend significantly on four main parameters: anode target material, the product of tube current and exposure time (mAs), tube potential (kVp), and beam filtration **[47].**

Briefly, the efficiency of bremsstrahlung production is proportional to Z and therefore high atomic number targets may be desirable. Low-Z targets may also be used, although at MV tube potentials where more photons in the diagnostic energy range can be harnessed to enhance MV imaging. Furthermore, x-ray fluence (the number of x-rays per unit area) is linearly dependent on mAs. The tube potential determines the quality of the x-ray spectrum; an increase in tube potential will increase the energy as well as the bremsstrahlung efficiency of the tube.

Exposure is proportional to the square of the tube potential, and thus to maintain the same exposure when increasing kVp, mAs must be lowered **[47]**.

Another parameter that influences x-ray output is filtration. Filters are placed in-between the incident x-rays and the object to be imaged to change the quantity and quality of the x-ray spectrum before imaging takes place. Filtration is useful as it preferentially removes low energy photons that may increase dose to the patient but not contribute to the imaging process. Finally, added filtration causes dose to decrease without a significant loss in image quality **[47]**.X-ray images are formed by placing a detector behind the attenuating material to measure the number of quanta remaining after interaction with the attenuating material . The discussion here is limited to modern x-ray detectors, however for a discussion of the history of x-ray detection the reader is referred to **[47]**.

The current technology used in x-ray detectors include flat panel thin-film transistor (TFT) array detectors. Direct detection involves the conversion of x-ray photons to ion pairs where a detector is biased by a potential creating an electric field that directs the ion pairs towards the TFT array. Indirect detection harnesses the ability of a scintillating material (e.g., Cesium Iodide (CsI)) to produce visible light photons when incident with x-rays. Photodiodes are then used to convert the light to a charge that is read by the TFT **[47].**

3.2 Volumetric imaging

3.2.1 CT generations

The first CT scanners had a single narrow pencil beam geometry with a single detector. They operated on the principle of rotation and translation mechanisms, as the x-ray tube and detector had to move around the entire object to attain the necessary projections. Since there was

only one ray per measurement, the acquisition was inherently slow; although one advantage was the significant scatter rejection.

The second generation of CT introduced fan beam collimation, where a multiple ray beam was collimated to a thin fan and made incident on more detectors. This generation maintained the same rotate/translate principle, and although the cost increased with more detectors, single slice acquisition times decreased from minutes to tens of seconds.

The third generation of CT employed a wider fan beam with a semi-arc of detectors that allowed for entire patient cross sections to be covered. The rotate/rotate design enabled patients to simply lie flat, while the imaging assembly rotated around, acquiring each slice on the order of seconds. Helical acquisitions could then also be performed with rotation of the x-ray tube and detector, while the patient bed translated, creating a helix pattern. Helical reconstruction algorithms assume x-rays have traced a circular path, and data must be interpolated into a series of axial images. This generation was significantly improved when the “slip ring” was introduced and removed the need for x-ray tube and detector assembly to be physically tied to the system with wires. The freedom of tube/detector rotation removed the need to perform a single rotation for every translation and allowed entire volumes to be acquired in tens of seconds.

The fourth generation of CT incorporated an entire ring of detectors, eliminating the need for detector rotation. It was designed to overcome the ring artifacts associated with third generation scanners if a detector element were to fail. The costs associated with many more detectors have led to a greater adoption of third generation scanners that perform post-processing to alleviate ring artifacts. Furthermore, fourth generation CT is known to deliver higher patient dose, which is less favourable in most diagnostic CT settings.

The major geometric changes were between the first and third generation scanners, as illustrated in figure 3.2:

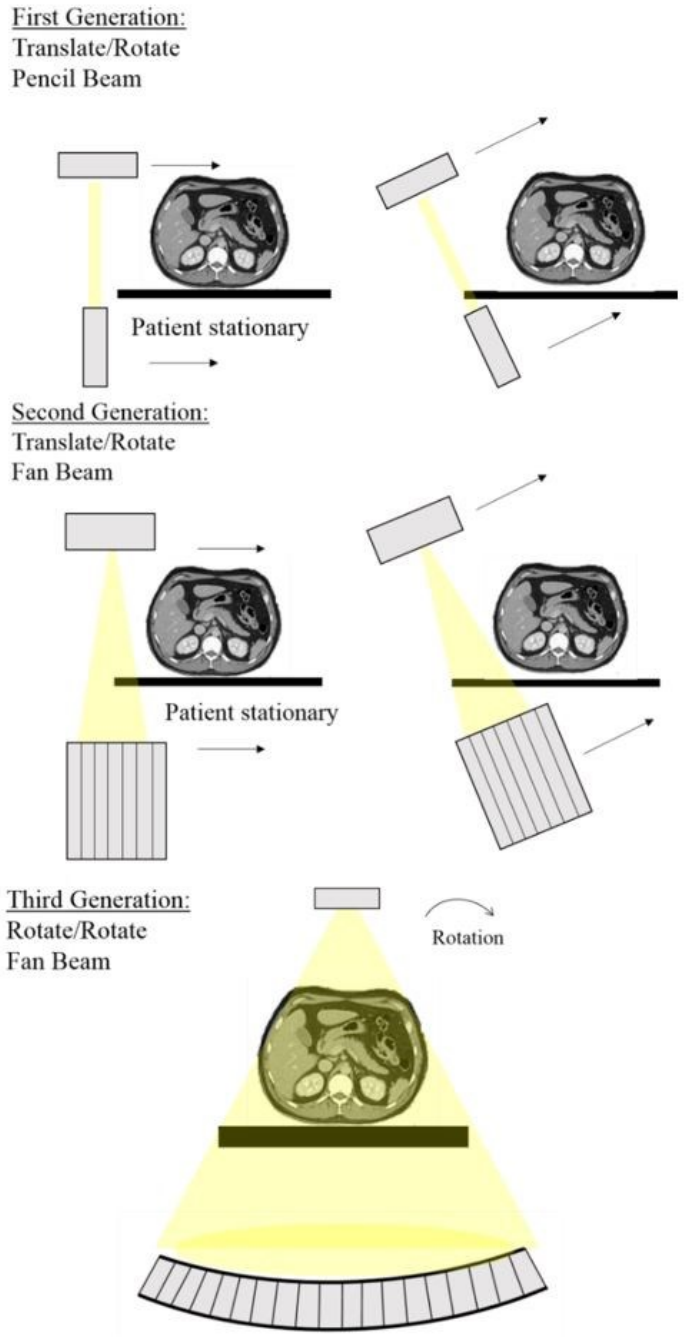

Figure 3.2: Illustrating a comparison of first three generations of CT to demonstrate the major changes in hardware and geometry.

3.2.2 Cone Beam CT

The cone beam geometry uses an x-ray source and a flat panel detector assembly that rotates around the patient. A circular electron beam is incident on an angled anode, emitting a cone of x-ray photons towards an object. A single cone beam projection is insufficient to complete the object's sinogram, however an algorithm proposed by Feldkamp, Davis, and Kress (FDK) **[21]** gives an accurate approximation based on filtered back projection. This algorithm is the most widely used for clinical CBCT image guidance.

CBCT acquisitions are performed to complete an object's sinogram at every angle on the domain 0 to π plus the fan angle. Acquisitions are also performed over a full 0 to 2π rotation, where the patient is centered about the axis of rotation. An illustration of a CBCT is shown in figure 3.3:

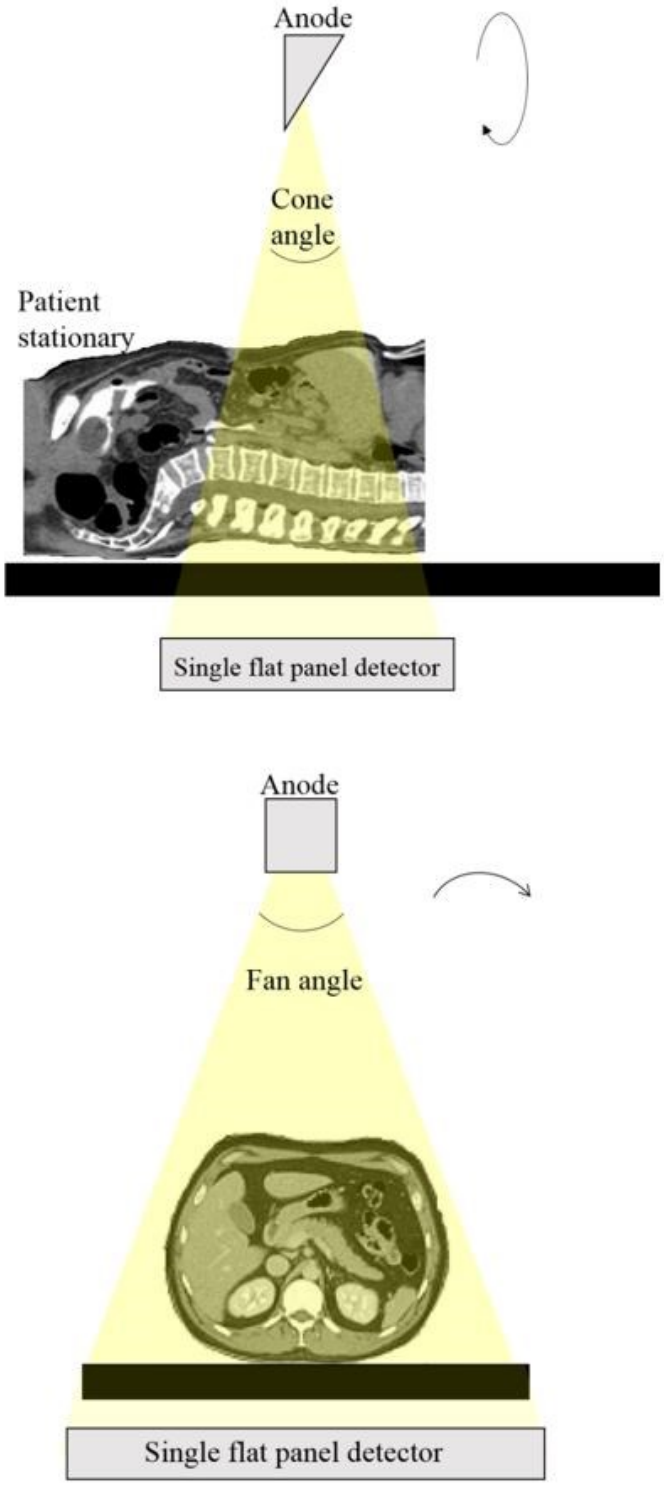

Figure 3.3: Illustrating the mechanism behind cone-beam CT acquisition for views demonstrating cone angle (top) and fan angle (bottom). In each case, rotational direction is given by the arrow.

These two types of acquisitions are commonly referred to as CBCT "modes". The acquisition that requires a rotation of 0 to π plus the fan angle, is called a "full-fan" acquisition mode, because the filter used is a full bowtie. The acquisition that requires a full 0 to 2π acquisition is called a "half-fan" acquisition mode because the filter is a half bowtie. Furthermore, half-fan acquisitions allow for larger field-of-view reconstructions. This is accomplished by laterally offsetting the detector panel so that projections are no longer redundant after π plus the fan angle. Bowtie filters shape the outgoing x-ray beam to enhance CBCT projections. They offer reduced skin dose to the patient, while reducing scatter and improving image quality. A full bowtie is more useful for imaging small anatomies such as a patient's head, whereas a half bowtie is useful for body scans. On TrueBeam®, both bowties are made of aluminum with a maximum profile thickness of 28 mm. An example comparing a full-fan to half-fan acquisition is illustrated in figure 3.4:

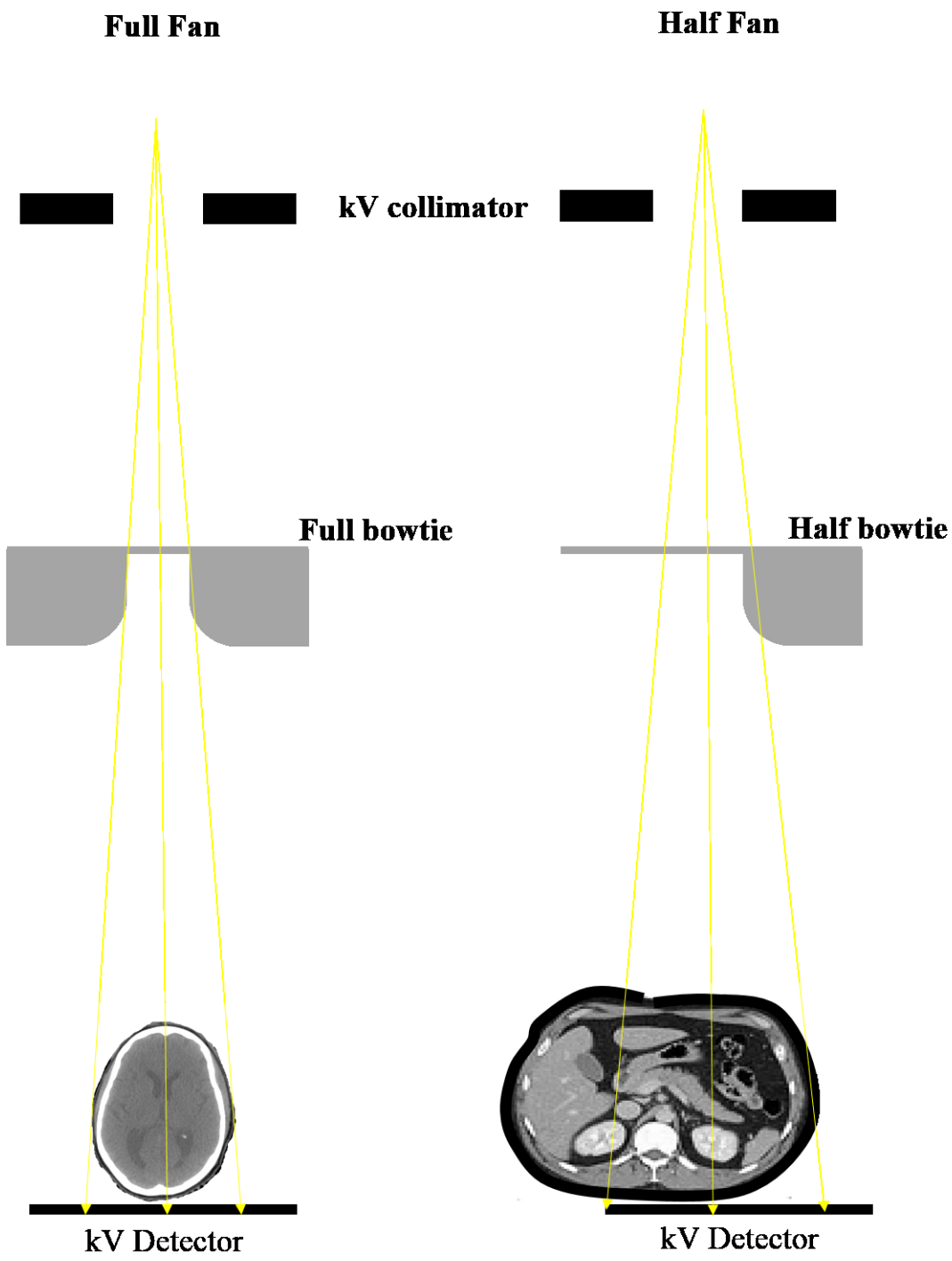

Figure 3.4: Illustrating example of full-fan acquisition geometry (left) and half-fan acquisition geometry (right). Full-fan does not require 0 to 2π acquisition compared to half-fan because projections are redundant after π +fan angle, however it is limited to scanning smaller objects.

Corrections must be applied to the raw cone beam projections after acquisition. The first are standard corrections of flood field, dark field, and pixel map correction. The first two corrections are applied to projections according to the equation:

$$I_{corrected} = \frac{I_{Raw} - I_{Dark}}{I_{Flood} - I_{Dark}} \tag{25}$$

In addition, a pixel map correction may be applied to correct for dead pixels in the detector, e.g., where the dead pixel value is replaced by the average of neighbouring pixels.

After these standard corrections are applied, two additional corrections are performed. The first, Feldkamp or Cosine weighting accounts for the fact that a circular cone is being projected onto a flat detector **[48]**. It corrects each projection by scaling to the normalized vector position of the pixel at the distance between source and detector. The second, Parker weighting, deals with overlapping data for scans less than 2π **[49]**. In both FBCT and CBCT, incomplete reconstructions occur for acquisitions of 0 to π, Therefore, all arcs are extended by the fan angle, however double scanned data can cause artifacts [**49]**. Parker weighting assigns weights to the image to mitigate the effects of redundant data.

The next step in the CBCT processing chain is to filter each projection, as illustrated for the example of the Shepp-Logan phantom in figure 3.5 below. Backprojection is then applied to generate the 3D image set. Further corrections may be applied before backprojection, such as the scatter correction and analytic spectrum correction algorithms employed by Varian™ **[50, 51]**. Briefly, the scatter correction algorithm of **[50]** uses an adaptive scatter kernel superposition in attempts to deconvolve scatter from projection images. The analytic spectrum correction is a look-up table for every pixel based on the beam quality and detector response that was validated with Monte Carlo **[51]**. These model-based correction algorithms are applied to the raw

projection data before backprojection. After backprojection, post-processing methods may be performed such as mapping to HU and ring-suppression **[52]**.

3.2.3 Volumetric CT reconstruction

Each ray in a 2D x-ray projection represents a line integral of attenuation coefficients. The complete collection of line integrals represents the Radon transform of the 2D distribution of attenuation coefficients in the imaged object. The Radon transform is thus described by the following equation:

$$R_\theta(p) = \ln\left(\frac{N_0}{N}\right) = \int_{-\infty}^{\infty}\int_{-\infty}^{\infty}\mu(x,y)\delta(x\cos\theta + y\sin\theta - p)dxdy \tag{26}$$

where $R_\theta(p)$ denotes the Radon transform at a position p and projection angle θ, while δ denotes the Dirac delta function **[53]**. If a Radon transform is performed at every projection angle a mathematical basis set is formed, also known as a sinogram.

An example of Radon transform and corresponding sinogram (domain 0 to π) is given for the Shepp-Logan phantom **[54]** in figure 3.5.

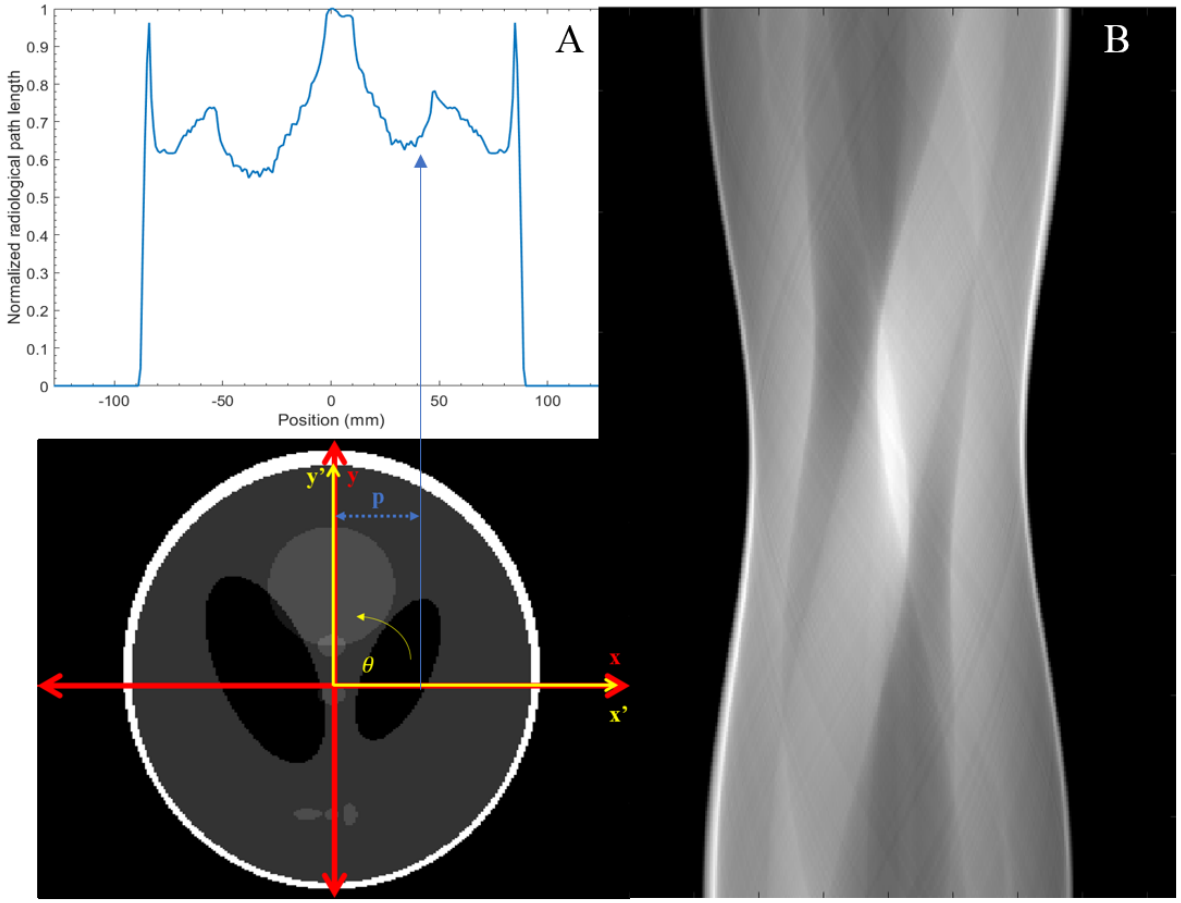

Figure 3.5: Illustrating Shepp-Logan phantom with corresponding Radon Transform at $\theta = 0$ radians where the rotated frame denoted by x'y' is equivalent to the original xy frame (A). The position is denoted by p of the rotated frame. The associated sinogram for all p and θ is given over the domain 0 to π (B).

Moreover, the following derivation is performed to relate the Radon transform to the Fourier transform. Let the Fourier transform of $\mu(x, y)$ be

$$\mathrm{M}(u, v) = \int_{-\infty}^{\infty}\int_{-\infty}^{\infty} \mu(x, y) e^{-2\pi i(ux+vy)} dxdy \tag{27}$$

where u and v are defined in the Fourier domain as the inverse quantities of x and y respectively measured in (mm^{-1}).

A substitution to polar coordinates is then performed by letting $u = r\cos\theta$ and $v = r\sin\theta$:

$$\mathrm{M}(r,\theta) = \int_{-\infty}^{\infty}\int_{-\infty}^{\infty}\mu(x,y)e^{-2\pi ri(x\cos\theta+y\sin\theta)}dxdy \tag{28}$$

The sifting property of the Dirac delta function states that any function *f(h)* can be sifted to a different position on that same function *f(h')* if the function is multiplied by the sifted Dirac delta function:

$$f(h') = \int_{-\infty}^{\infty} f(h)\delta(h-h')dh \tag{29}$$

This property can then be applied here letting *f(h)* be sifted Fourier transform:

$$e^{-2\pi ri(x\cos\theta+y\sin\theta)} = \int_{-\infty}^{\infty} e^{-2\pi rip}\delta(x\cos\theta + y\sin\theta - p)dp \tag{30}$$

A substitution is then made into equation 28:

$$\mathrm{M}(r,\theta) = \int_{-\infty}^{\infty}\int_{-\infty}^{\infty}\int_{-\infty}^{\infty}\mu(x,y)e^{-2\pi rip}\delta(x\cos\theta + y\sin\theta - p)dxdydp \tag{31}$$

This is simply the Fourier transform of the original Radon transform:

$$\mathrm{M}(r,\theta) = \int_{-\infty}^{\infty} R_\theta(p)e^{-2\pi rip}dp \tag{32}$$

The properties of the Fourier transform thus demonstrates a relationship between the 1D Fourier transform of an object at specific angle θ, and the Radon transform at that same angle:

$$\mathrm{M}(r,\theta) = F[R_\theta(p)] \tag{33}$$

$$R_\theta(p) = F^{-1}[\mathrm{M}(r,\theta)] \tag{34}$$

where *F* and F^{-1} are the Fourier and inverse Fourier transforms respectively. The relations of 33 and 34 are well known as the *Fourier Slice theorem* or *projection slice theorem*. It is used to reconstruct $\mu(x,y)$ by operating in the Fourier domain, and then performing the inverse transform to recover the coefficient map.

Furthermore, this theorem is used in backprojection which is roughly defined as a "smearing back" procedure of an x-ray projection across the image at the specific projection angle θ **[53]**. The "smearing" is a function of the projection integral discussed above:

$$\mu(x,y) = \int_0^{\pi} \int_{-\infty}^{\infty} R_\theta(p)\delta(x\cos\theta + y\sin\theta - p)dpd\theta \tag{35}$$

Substituting the Fourier slice theorem into equation 34 yields:

$$\mu(x,y) = \int_0^{\pi} \int_{-\infty}^{\infty} \int_0^{\infty} \mathrm{M}(r,\theta)e^{2\pi rip}\delta(x\cos\theta + y\sin\theta - p)drdpd\theta \tag{36}$$

Applying the sifting property of equation 28 yields:

$$\mu(x,y) = \int_0^{\pi} \int_0^{\infty} \mathrm{M}(r,\theta)e^{2\pi ri(x\cos\theta + y\sin\theta)}drd\theta \tag{37}$$

Simply backprojecting the attenuation map yields a blurry image because bright pixel intensities are "smeared" across the entire image instead of being restricted to their origin. This problem is solved by filtering the projection data before it is backprojected; performed mathematically by multiplying a filtration function *r*:

$$\mu(x,y) = \int_0^{\pi} \int_0^{\infty} \mathrm{M}(r,\theta)e^{2\pi ri(x\cos\theta + y\sin\theta)}rdrd\theta \tag{38}$$

This multiplication must then follow through the reconstruction chain:

$$\mu(x,y) = \int_0^{\pi} \int_{-\infty}^{\infty} \left[\int_0^{\infty} \left[\int_{-\infty}^{\infty} R_\theta(p)e^{-2\pi rip}dp\right]|r|e^{2\pi rip}dr\right]\delta(x\cos\theta + y\sin\theta - p)dpd\theta \tag{39}$$

which is equivalent to:

$$\mu(x,y) = \int_0^{\pi} \int_{-\infty}^{\infty} F^{-1}[F[R_\theta(p)]|r|]\delta(x\cos\theta + y\sin\theta - p)dpd\theta \tag{40}$$

An example of filtered compared to standard backprojection is illustrated for the Shepp-Logan phantom **[54]**, in figure 3.6 for commonly used filters:

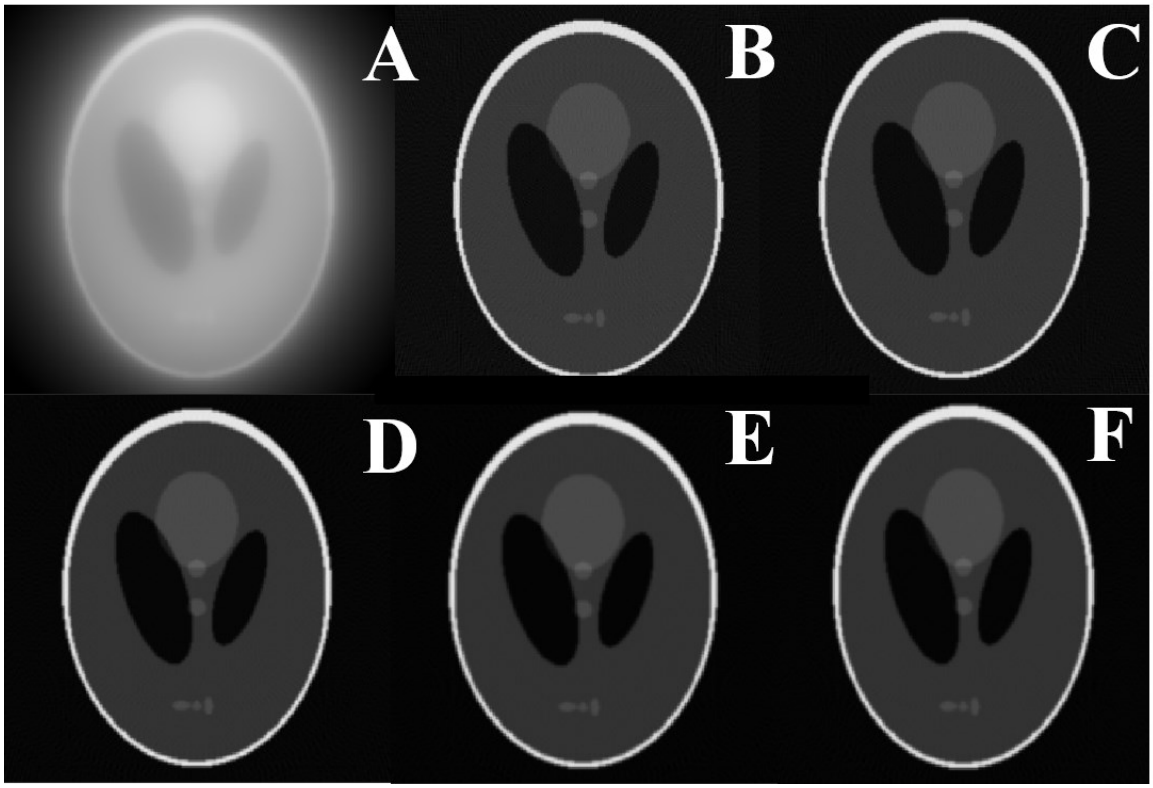

Figure 3.6: Illustrating the standard backprojection (A) compared to the ramp (B), Shepp-Logan (C), Cosine (D), Hanning (E), and Hamming (F), filtered backprojections of the Shepp-Logan phantom from 0 to π.

3.3 Contributions to Image quality

3.3.1 Contrast

The human body is made up of a variety of tissues with varying compositions and densities. As demonstrated in the previous chapters, interaction probabilities (attenuation coefficients) are largely dependent on the composition and density of matter. X-rays attenuate through matter following exponential attenuation in accordance with Beer's law:

$$N = N_0 e^{-\mu t} \tag{41}$$

where N_0 is the initial number of photons, μ is the linear attenuation measured in cm^{-1} and t is the thickness of the medium. The differential attenuation of the human body is illustrated by the concept of subject contrast in figure 3.7:

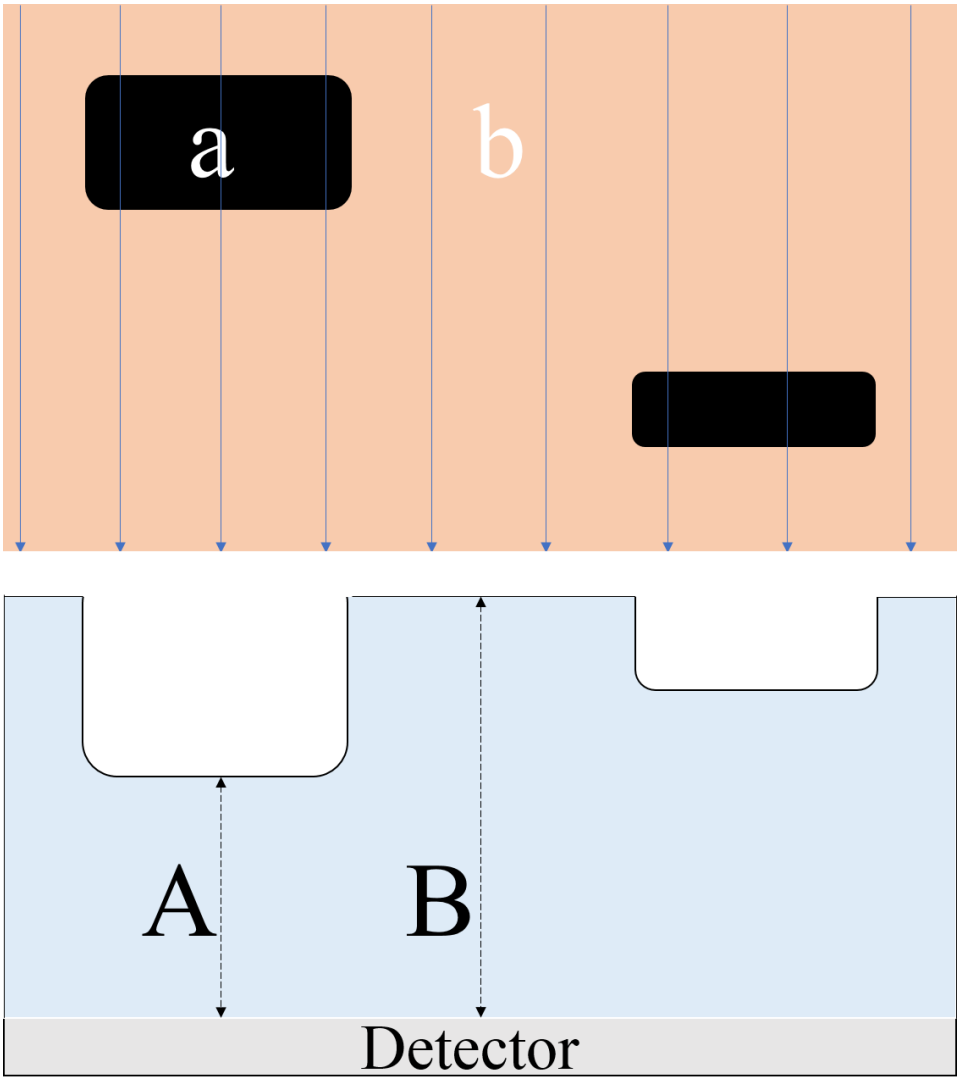

Figure 3.7: Illustrating the concept of subject contrast for the simple case of 2 differential attenuating media (a, b) Rays passing through the object (top) will give a profile before reaching the detector (bottom) whose height (A, B) will differ in accordance with the varying densities of the object.

$$C_{subject} = \frac{\bar{q}_A - \bar{q}_B}{\bar{q}_B} \tag{42}$$

where $\bar{q}_A$ is the average number of x-rays (quanta) remaining after interacting with medium *A* and $\bar{q}_B$is the average number of quanta remaining after interacting with medium B.

3.3.2 Noise

Noise can be grouped into two separate categories: quantum noise, and noise from scatter. Quantum noise is Poisson distributed, referring to the probability of several independent (random) events in a fixed interval of space or time. It is thus clear that quantum noise depends on the number of x-ray photons interacting with the detector, making it a function of x-ray tube parameters that influence output. Assuming that *N* photons reach a given pixel, the quantum noise is defined to be **[47]**:

$$\sigma = \sqrt{N} \tag{43}$$

The relative noise is then defined as the ratio of noise to the total number of photons:

$$\frac{\sigma}{N} = \frac{\sqrt{N}}{N} = N^{-\frac{1}{2}} \tag{44}$$

Conversely, the ratio of total number of photons (signal) to the amount of noise σ is aptly named the signal-to-noise ratio (SNR), obtained by inverting equation 44 as follows:

$$SNR = \frac{N}{\sigma} = \frac{N}{\sqrt{N}} = N^{\frac{1}{2}} \tag{45}$$

Equation 45 gives the ideal SNR for *N* photons incident on a detector; however, a quantity called the quantum detection efficiency (QDE) (*n*) will influence *N* according to

$$n = 1 - e^{-\mu t} \tag{46}$$

where μ is the attenuation coefficient associated with the detector material, and t is the thickness of the detector material. This implies that SNR must account for QDE, through a multiplication by n:

$$SNR = n(N)^{\frac{1}{2}} \tag{47}$$

It is important to note that equation 47 implies that the SNR is dependent on the number of photons reaching the detector, which may be controlled by varying the x-ray tube current. Furthermore, SNR is dependent on the QDE which in turn depends on the linear attenuation coefficient, which depends on the x-ray spectrum energy. The x-ray tube potential controls the spectrum's energy and therefore, the image quality metric SNR depends on both tube current (mA) and tube potential (kVp).

Another useful image quality metric is known as the contrast-to-noise ratio (CNR):

$$CNR = \frac{|\bar{S}_{ROI} - \bar{S}_B|}{\sigma_B} \tag{48}$$

where S_{ROI} denotes the average signal intensity in a specific region of interest (ROI), S_B denotes the average signal intensity in the background of the image, and σ_B denotes the noise in the background of the image. This metric is practically useful when comparing different regions in an image.

3.3.2 Scatter in medical images

Variations in detected signal intensity may also be attributed to scattered radiation reaching a pixel on the detector from a non-primary x-ray. The measured detector signal from a scattered x-ray is also known as a secondary signal. Therefore, the amount of scatter in a medical

image can be quantified according to the ratio of primary photons reaching the detector to the number of secondary photons from scatter (SPR). The main source of scatter in medical images of the human anatomy occur from Compton scattering events in soft tissue. The low effective atomic number of tissue decreases the probability of photoelectric interactions in the diagnostic x-ray range. Noise from scatter is known to increase with the radiation field size and patient thickness, thus lowering image quality.

Scatter also significantly hinders image quality in CBCT as compared to FBCT. Siewerdsen and Jaffray **[55]** showed that when increasing the cone-angle, the SPR also increased by 17.7% per degree in a uniform cylindrical phantom. As cone-angle increases, the total irradiated area also increases. In a patient, this results in significantly more Compton interactions in tissue, and thus more scatter. The scattered photons obey the K-N cross section formalism which demonstrates more backwards scatter for lower energy incident x-rays, like in the diagnostic range **[40]**. This results in lower signal at the center of a detector plane, and appears as shading, also known as scatter based "cupping". Most commercial CBCT systems use a cone angle of approximately 10°, whereas the cone-angle for commercial FBCT systems have a cone angle on the order of 1° or less with multiple detectors that improve primary detection. Therefore, it is expected that CBCT image quality should be hindered significantly more than FBCT due to increased scatter detection, if scatter corrections are not applied.

Techniques used to reduce the effects of scatter can be divided into analytical solutions and hardware solutions. Analytical scatter correction techniques aim to model scatter and account for it in specific geometries. The gold standard to model these geometries is with Monte Carlo methods, to accurately simulate radiation transport. Common hardware solutions employ collimation techniques that decrease the irradiated area, filtration (bowtie filter), and the anti-

scatter grid. Anti-scatter grids are designed to permit primary photons through the grid, while attenuating scattered photons to not reach the detector **[47]**.

3.3.3 Rose criterion

Albert Rose defined signal as the change in number of image quanta from an object, being integrated over the entire area of an object **[56]**. Using a similar equation to subject contrast (42):

$$C = \frac{\bar{q}_B - \bar{q}_{ROI}}{\bar{q}_B} \rightarrow \Delta S = (\bar{q}_B - \bar{q}_{ROI}) \int_0^A dA \tag{49}$$

where $\bar{q}_B$ denotes the average number of quanta per unit area measured in the background region, $\bar{q}_{ROI}$ is average number of quanta measured in the ROI per unit area, and ΔS is called the "signal difference" between the two quantities. The quantity is then multiplied by the total image area A.

From equation 44, this makes the *SNR* for uncorrelated Poisson noise:

$$SNR_{ROSE} = \frac{A(\bar{q}_B - \bar{q}_{ROI})}{\sqrt{\bar{q}_B A}} = C\sqrt{\bar{q}_B A} \tag{50}$$

Rose cited a relationship of the human eye's capability to discern signal in a medical image at a SNR_{Rose} of 5 well known as the Rose Criterion **[56]**. Furthermore, the human eye should be able to discern contrast differences in a medical image between CNR of 3 – 5; this is known as the Rose Criterion for CNR **[56]**. The lower limit of CNR_{Rose} was used for assessing adequate image quality for this research. This criterion is based on the Rose model of noise, which is thus limited by two fundamental assumptions. First, the model assumes that in the presence of signal the variance is equal to the mean total variance of signal and background. This assumption is only valid if the signal variance is much smaller than the background variance,

which would be the case for low-contrast signals **[57]**. Second, as mentioned in previous sections, photon noise is Poisson distributed. The assumption that Poisson noise can be approximated by Gaussian noise is only true when photon densities are sufficiently large. A comprehensive discussion on how to attain these constant values can be found in Albert Rose's *Vision: Human and Electronic* **[56]**.

3.4 Contrast agents in radiotherapy

As discussed in chapter 2, diagnostic x-rays will preferentially interact due to the photoelectric effect given sufficiently high atomic number, and the probability of interaction increases as the photon energy just exceeds the k-edge energy specific to an absorbing element. Common contrast agents used in radiotherapy are: iodine (k-edge = 33.2 keV), and barium (k-edge = 37.4 keV). Iodine is commonly used to enhance helical FBCT diagnostic imaging because its short time course in the body is appropriate for fast imaging protocols. Barium is used in the "Barium Swallow" procedure, used to diagnose problems with the digestive system. In this case continuous x-ray imaging can be performed to track the contrast agent's progress throughout the body. Gadolinium (k-edge = 50.2 keV) has promising attenuating properties because of its high atomic number. As discussed previously, while Gd-based compounds (e.g. Primovist) have been investigated in the context of CT imaging **[38, 39]**, in general no demand has existed for FBCT due to the adequacy of I-based agents. The time-course of CBCT acquisition, on the other hand, necessitates a compound that remains in the imaged anatomy for minutes.

Other research has also concerned the use of nanoparticles as contrast agents for radiotherapy. These uses include gold ($Z_{Au} = 79$) and gadolinium nanoparticles **[58]**. Regardless of the use, the

theory remains the same: in the diagnostic x-ray range, increased contrast is obtained for higher Z materials at lower energies due to the increased probability of the photoelectric effect.

3.5 Image artifacts

While many artifacts may be produced in CT imaging, discussion in this section is limited to artifacts experienced in the course of this research. Most artifacts were readily corrected owing to calibrations or post-processing techniques, however, as shown in the results section, some artifacts remained unresolved.

The first artifact encountered is demonstrated in figure 3.8 with a uniform low attenuating region at the center of the image.

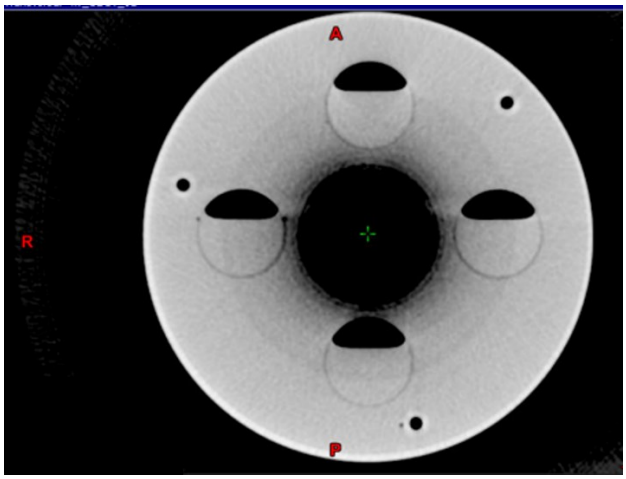

Figure 3.8: Artifact for 80 kV, 1080 mAs, full-fan bowtie half-arc acquisition, resulting from improper air norm calibration.

The artifact was mitigated upon updating the air normalization calibration and was therefore deemed to be caused by an improperly calibrated detector element. The artifact would have resulted from each projection being log-normalized by the incorrect projection before backprojection, and then backprojecting the mistake through the rest of the reconstruction.

The second artifact was a crescent artifact with a highly attenuating crescent on one side of the image, and a correspondingly low attenuating crescent on the other side. The artifact is illustrated in figure 3.9.

Figure 3.9: Crescent artifact for 140 kV, 2000 mAs, full-fan bowtie half-arc acquisition, resulting from improper crescent calibration.

Crescent artifacts occur when there is a discrepancy in the geometric position of the bowtie filter relative to the default or previous calibration. The calibration is performed in air to measure the amount of gravitational "bowtie sag" as the gantry travels the required range and compensated for by adjusting the air norm chamber **[59]**. The artifact was mitigated after performing the crescent calibration.

The third artifact observed was "cupping" caused by beam hardening. This phenomenon occurs as a beam passes through an object and low energy photons are rapidly absorbed, making the average energy of the beam higher, and thus "harder" (more penetrating) **[60]**. Furthermore, this

effect was exacerbated by scatter induced cupping which was described in the previous section. In a cylindrical geometry such as that used in this work, this results in a lower intensity cup effect. An example of the cupping artifact is illustrated in figure 3.10.

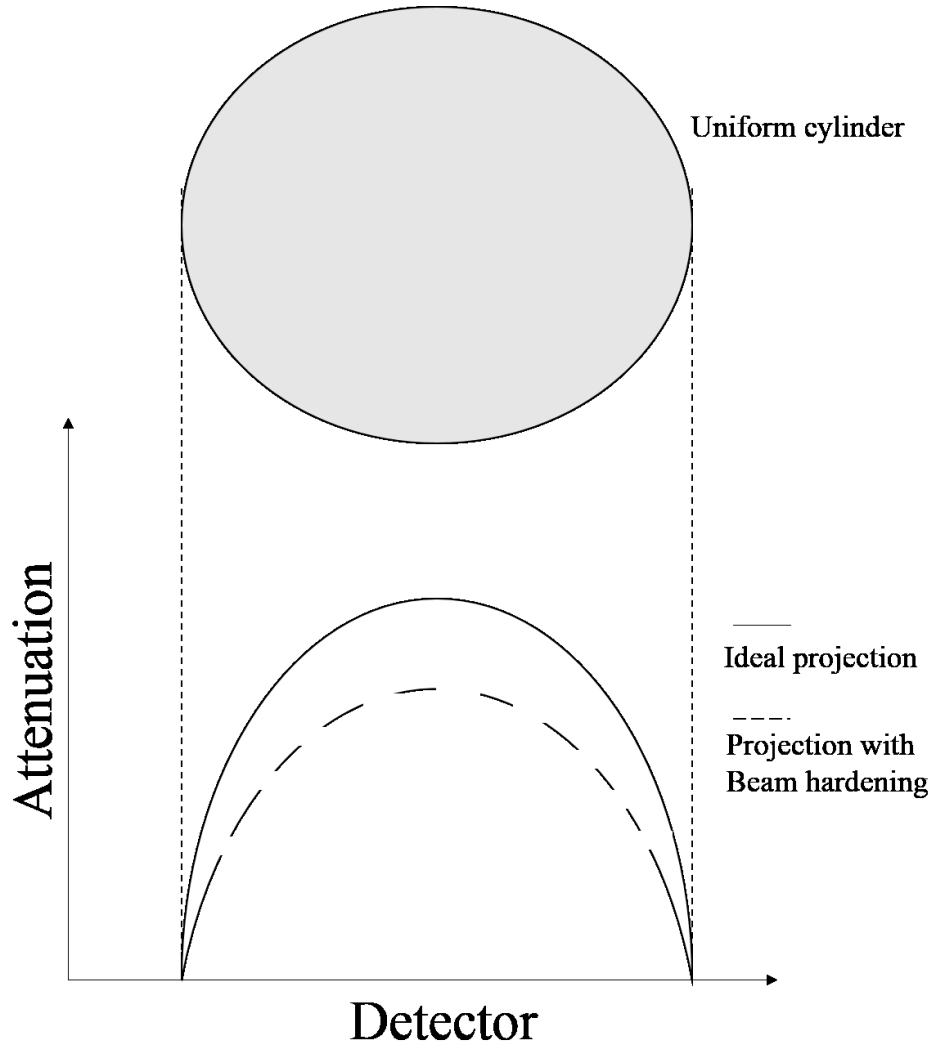

Figure 3.10: Illustrating the theory behind cupping artifacts in a uniform water cylinder. An ideal projection is depicted with the solid line, and the projection after beam hardening is given by the dashed line.

This was mitigated to a certain extent for clinical CBCT modes, but difficult to overcome with non-clinical CBCT. As discussed in the previous section, Varian™ applies an analytic spectrum

correction on clinical CBCT projection data. Future chapters will demonstrate the significant effect of beam hardening on the data acquired for this dissertation.

Chapter 4 Methods and Materials

4.1 Phantom preparation

4.1.1 Sample preparation

Five different concentrations were investigated based on liver concentrations of the contrast medium, derived from Schmitz *et al.* **[32, 38, 39]**, as well as the toxicity results established in the product monograph for Primovist® **[33]**. These concentrations were 0.0125, 0.025, 0.05, 0.075 and 0.1 mmol/kg, corresponding to expected concentrations in the liver after administrations of 1, 2, 4, 6, and 8 times the Primovist® monograph-recommended dose. The relationship between administered concentration and expected concentration in the liver can be expressed with the following relation:

$$C_L \left[\frac{mmol}{kg}\right] = C_A \left[\frac{mmol}{kg}\right] * U \tag{51}$$

Where C_L and C_A are the expected liver concentration and administration concentration expressed in mmol/kg BW; and U is the uptake factor given a constant value of 0.5 to account for the proportion of the drug in the liver **[33]**.

Each concentration was diluted from the manufacturer provided stock solution of 0.25 mmol/mL and stored in a 60 mL cylindrical specimen container (NCS Diagnostics Incorporated, Etobicoke, Canada).

The diluted concentration was hypothesized to be representative of the expected concentration in the liver. The true concentration in the liver is entirely dependent on the patient specific pharmacokinetics, however an approximation was made for the purposes of this experiment. It is well-known that the concentration (molarity) of any solution is a ratio of the

total amount of substance (mols) to the volume of solution. Given that the contrast agent is administered as a ratio of the total number of mols to the patient's body weight, a relation between administered dose and diluted concentration (C_D) was required.

$$C_D\left[\frac{mmol}{mL}\right] = \frac{C_A\left[\frac{mmol}{kg}\right] * U * BW\ [kg]}{V_L\ [mL]} = \frac{C_L\left[\frac{mmol}{kg}\right] * BW\ [kg]}{V_L\ [mL]} \tag{52}$$

Equation 52 illustrates that the number of mols of contrast injected into the body can be obtained by multiplying the administered dose by the patient's body weight. The pharmacokinetics cited in the Primovist® product monograph **[33]** are described for various animal models and human models from clinical trials. The drug elimination studies performed in humans, state equal elimination through the renal (~50%) and hepatobiliary (~50%) systems. Assuming half the contrast goes to the liver **[33]**, the total number of moles is simply multiplied by the uptake factor. Furthermore, assuming a liver volume permits the calculation of the necessary dilution concentration.

Given the well-known dilution equation that assumes mass conservation in terms of the moles of the stock solution, one can rearrange to solve for the volume of stock solution required to achieve the diluted concentration from equation 53:

$$n_S = C_S V_S = n_D = C_D V_D \tag{53}$$

$$V_S = \frac{C_L\left[\frac{mmol}{kg}\right] * BW[kg] * V_D[mL]}{C_S V_L}$$

Where the subscript *S* denotes the stock solution, *D* denotes the dilution, and *L* denotes the liver. The variables: *BW* and V_L are largely patient dependent as they will influence the pharmacokinetics of the contrast agent. To simplify this work in terms of maximizing use of the

provided contrast material, BW was assumed to be 100 kg, while the average volume of the human liver was estimated from results of Suzuki *et al.* to be 1600 mL **[61]**. A sample calculation is provided in equation 54 assuming dilution to the recommended dose:

$$V_S = \frac{0.0125\ \left[\frac{mmol}{kg}\right] * 100\ [kg] * 60\ [mL]}{0.25\ \left[\frac{mmol}{mL}\right] * 1600\ [mL]} = 0.19\ [mL] \tag{54}$$

Therefore, to dilute to a 60 mL concentration of the recommended dose of 0.025 mmol/kg, the solution was prepared with 59.81 mL water and 0.19 mL Gadoxetate Disodium. Volume measurements were made with 60, 10, and 1 mL syringes (Becton Dickinson, Oakville, Canada).

4.1.2 Phantom geometries

Similar to work by Parsons and Robar **[62],** a cylindrical water phantom was machined by creating a Lexan (A&C Plastics Inc., Illinois, USA) shell, of diameter 22.2 cm and length 20 cm. The phantom housed a circular stage of diameter 20.5 cm with holes drilled to support five 4.0 cm diameter inserts of varying Gadoxetate Disodium concentration. The volume of the phantom was filled with water. This phantom, similar in diameter to other phantoms used for CBCT contrast assessment, was deemed a “best case” geometry with regard to subject contrast. Next, an ellipsoidal water phantom, also with a Lexan shell, was fabricated with a geometry more representative of the abdomen. The phantom had dimensions of 30.9 cm laterally and 22.3 cm in the anterior-posterior dimension, with a length of 21.5 cm. The phantom contained a similar arrangement of contrast containers as the cylindrical phantom. A photo of both contrast phantoms is shown in figure 4.1.

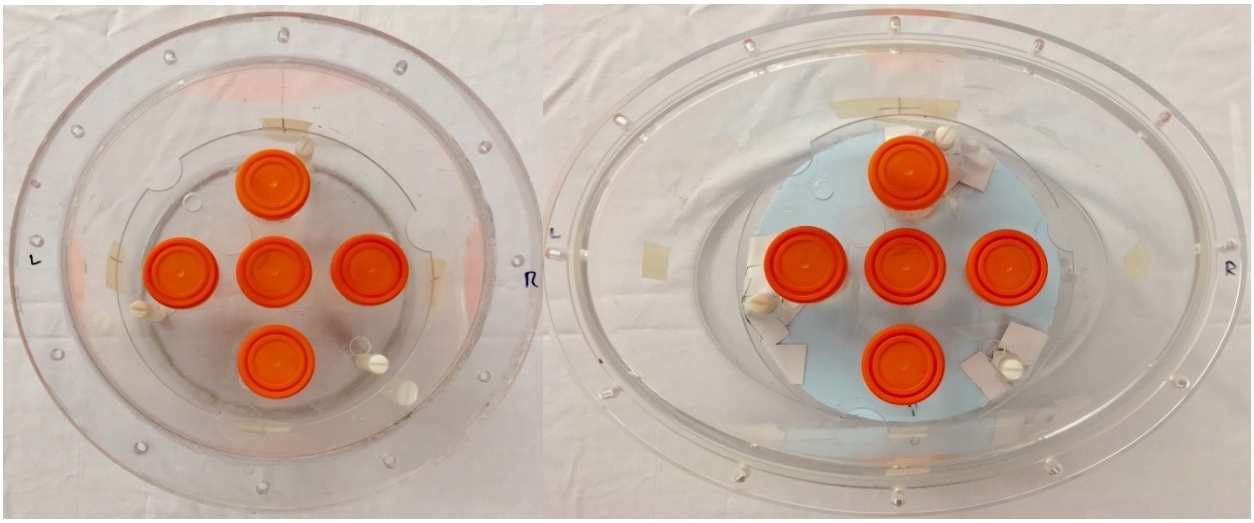

Figure 4.1: Cylindrical (left) and ellipsoidal (right) phantoms with contrast inserts.

4.2 Fan-Beam CT imaging

Given that all previous investigations were performed with a fan-beam geometry **[38, 39, 63]**, FBCT image data was acquired as a baseline and to provide data from current CT technology. A General Electric Discovery Series CT Simulator (GE Healthcare, Boston MA, USA) was used for all imaging.

For both cylindrical and ellipsoidal phantoms, a clinical abdomen protocol was chosen with reconstruction field-of-view (FOV) equal to 65 cm and voxel dimensions of 1.3 x 1.3 x 2.5 mm^3. A fixed tube current of 500 mA was set with an exposure time of 9.2 s, to give a total exposure of 4600 mAs. Each reconstruction was binned into 102 axial slices, giving approximately 45 mAs per slice. Tube potential was varied to include all possible options on board the unit: 80, 100, 120, and 140 kVp.

4.3 Cone-Beam CT Imaging

4.3.1 Clinical CBCT

As image quality with a cone-beam geometry is known to suffer due to the large solid angle for acceptance of scattered radiation compared to FBCT **[51, 64]**, it was hypothesized that CNR of the contrast agent would be inferior with this approach. All CBCT image data were acquired using a Truebeam 2.0 STx platform (Varian Medical Systems Inc., Palo Alto, CA, USA) with a source-to-imager (SID) of 150 cm. For this experiment tube potential and acquisition mode (i.e. full-fan vs. half-fan) were first varied, and then for the optimal combination, exposure was varied. To control these parameters, TrueBeam® service mode was used to create custom CBCT modes. As described in the TrueBeam® imaging manual **[65]**, the "CBCT Mode Editor" tab was used to copy existing modes and change relevant parameters. This is demonstrated in figure 4.2 for the case of a research mode based on a copied half-fan acquisition.

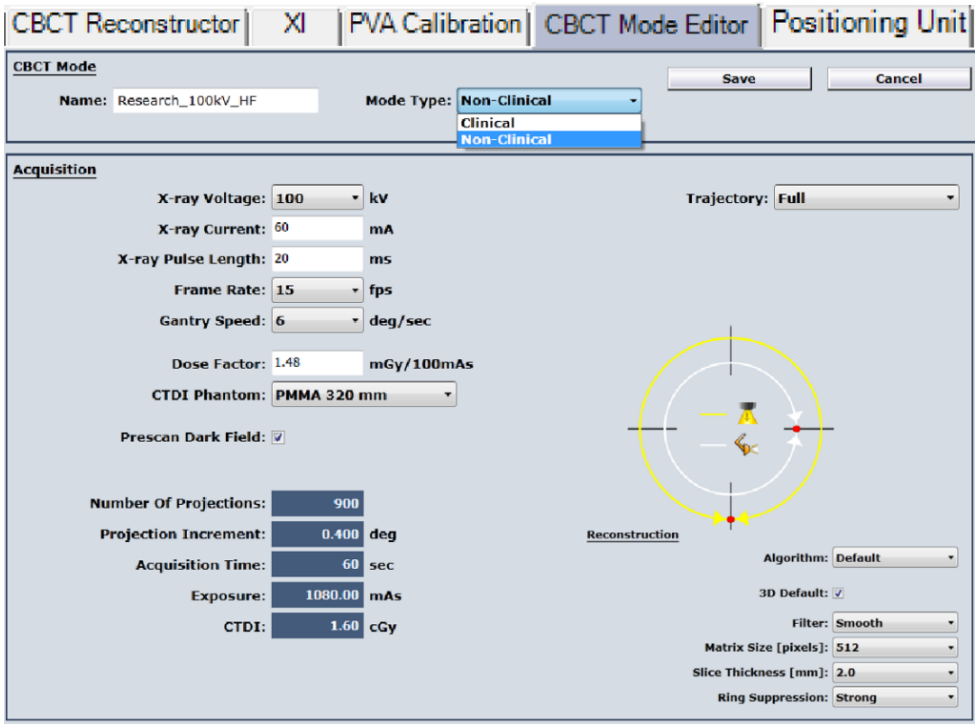

Figure 4.2: CBCT Mode Editor tab in service mode for an example CBCT mode that performs a half-fan acquisition with 100 kV tube potential and other parameters discussed in **[65].**

Changing the "Mode Type" from "Non-Clinical" to "Clinical" permits the acquisition in treatment mode. This methodology was repeated to create 12 research modes for this work with four clinical tube potentials for three acquisition types: half-fan full arc (HF-FA), full-fan half arc (FF-HA), and full-fan full arc (FF-FA). HF-FA acquisitions were based on the "Pelvis" clinical CBCT mode, while FF-HA was based on the "Head" mode. FF-FA was attained by changing the trajectory in "Head" from "Half" to "Full".

Prior to reconstruction, mode-specific dark field, flood field, and pixel corrections were applied, as well as crescent, air normalization, and HU mapping **[65]**. These corrections were based on calibrations performed using the "PVA Calibration" tab before acquisition as shown in figure 4.3:

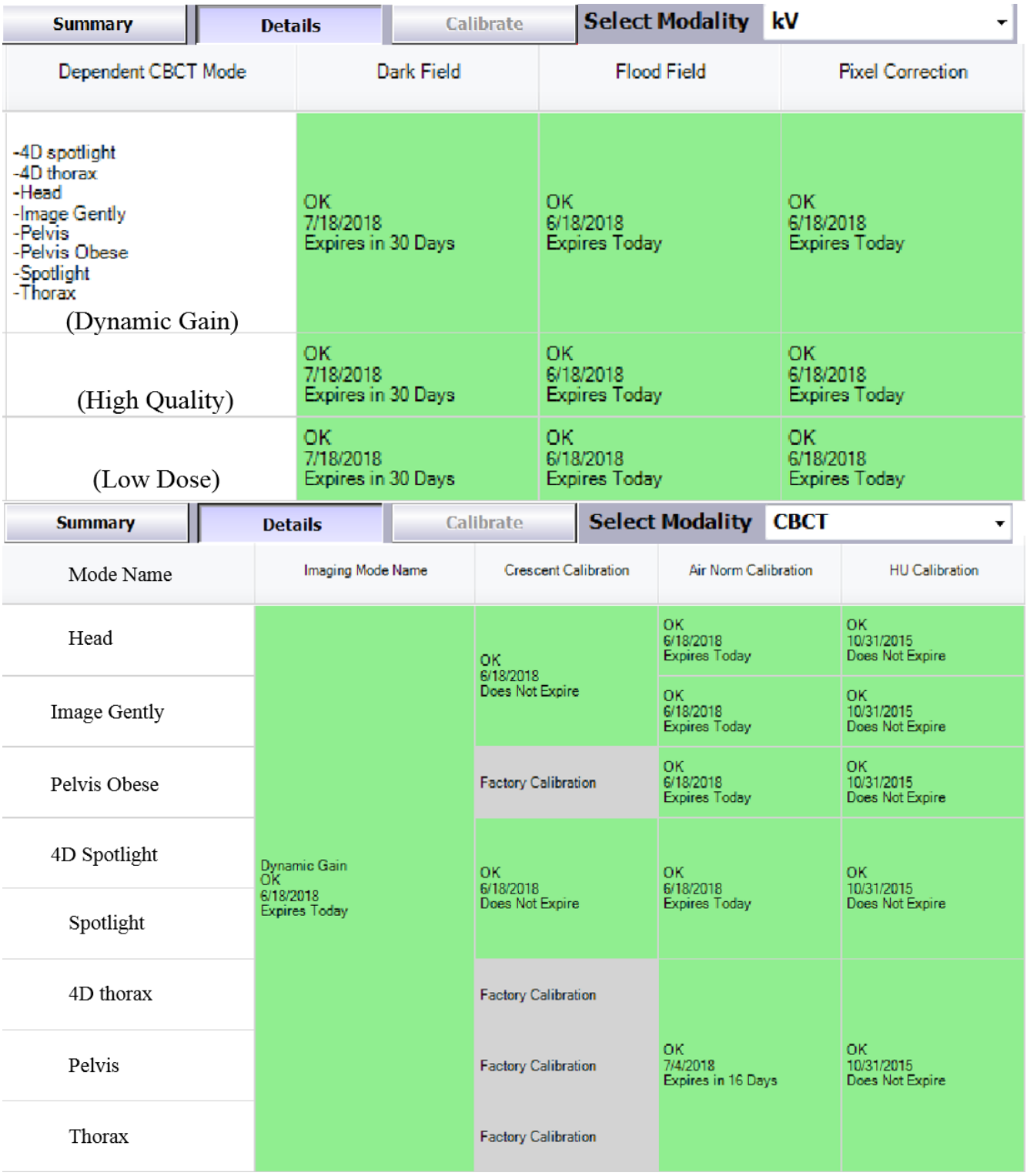

Figure 4.3: An example of the "PVA Calibration" options in service mode with only clinical modes available. Selecting an individual calibration permits the user to perform relevant the calibration procedure as described in **[65]**.

The default filtered backprojection reconstruction was used as proposed by Feldkamp, Davis and Kress **[22]**. Imaging was first performed on both phantoms for a fixed exposure of 1.2 mAs per projection (60 mA and 20 ms), while varying the clinically available tube potential and acquisition options. Once the best kVp and acquisition mode options were identified, exposure was varied to also examine the effect of this parameter on image quality. For each protocol, a water-only scan was also acquired to obtain the image background at the same location within the phantom and FOV, for use in the calculation of CNR.

4.3.2 Non-clinical CBCT

In treatment mode it is possible to acquire kilovoltage fluoroscopic images in the range of 40-140 kV in integer increments. However, the CBCT modes in this setting are limited to 80, 100, 125, and 140 kVp. Given this limitation, it was also desirable to perform an investigation of CBCT with tube potentials outside the clinically available range. The entire range of tube potentials was investigated in increments of 10 kV, not including the clinical 80, 100, and 140 kVp modes.

The calibration methods discussed above are conveniently performed for all clinical CBCT modes as part of the manufacturer's preventative maintenance. However, because this work investigated non-clinical "modes", a new methodology was required for calibration and reconstruction.

Calibrations of non-clinical modes were all performed in service mode using the XI (X-ray Imaging) node. This node is a computational sub-system of TrueBeam® that connects all functionality associated with x-ray imaging. As discussed in the previous section, CBCT modes based on clinically available parameters can be calibrated in service mode using the "PVA

Calibration" node. A similar workflow can be followed to obtain the necessary tube potential dependent calibrations. The HU calibration was deemed unnecessary as CNR is a measure of relative signal, regardless whether the signal has been converted to the HU scale. The crescent calibration was deemed unnecessary after personal communication with Varian™ service engineers **[66]** who advised that only the "Factory Default" calibration should be used for the type of acquisitions that were being performed (HF-FA). Therefore, the only necessary calibration to perform was the Air Normalization calibration. The acquisition procedure followed input parameters as demonstrated in figure 4.4.

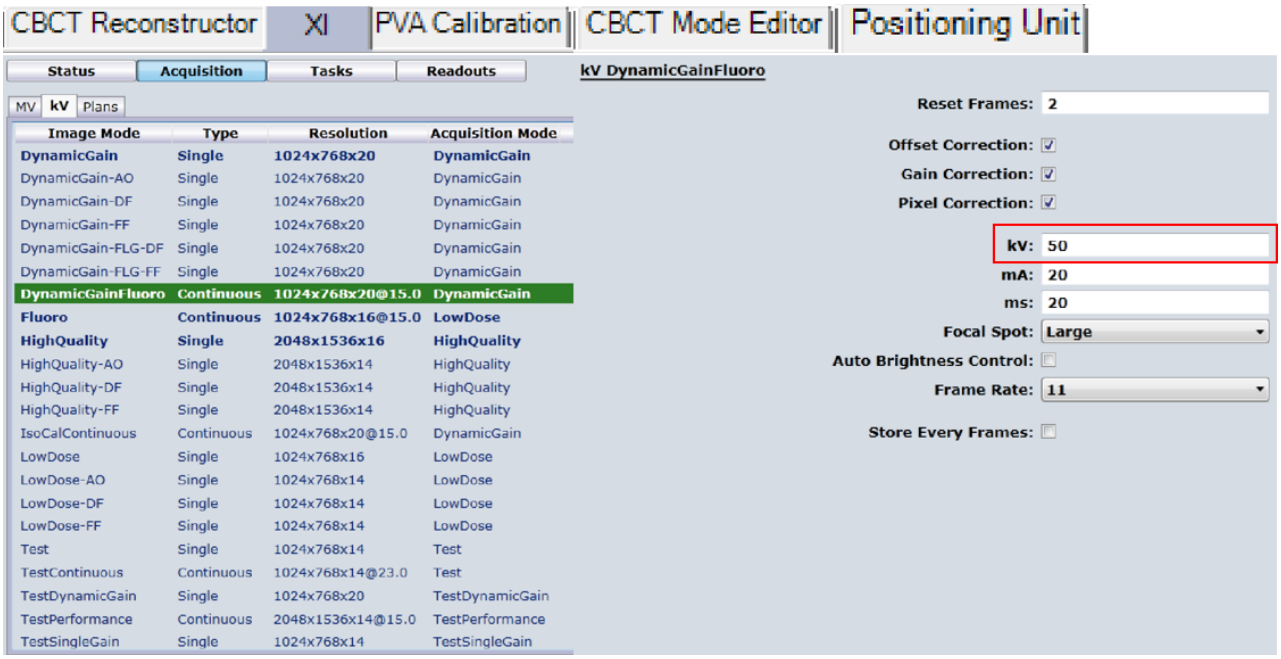

Figure 4.4: An example of the non-clinical Air Normalization calibration. All parameters in the figure remained constant, except for changing tube potential illustrated in red.

Approximately 100 frames were saved to average, with and without the half-fan bowtie filtration, and corresponding clinical kV collimator positions. These were verified by inspection, using the "Positioning Unit" tab, as shown in figure 4.5.

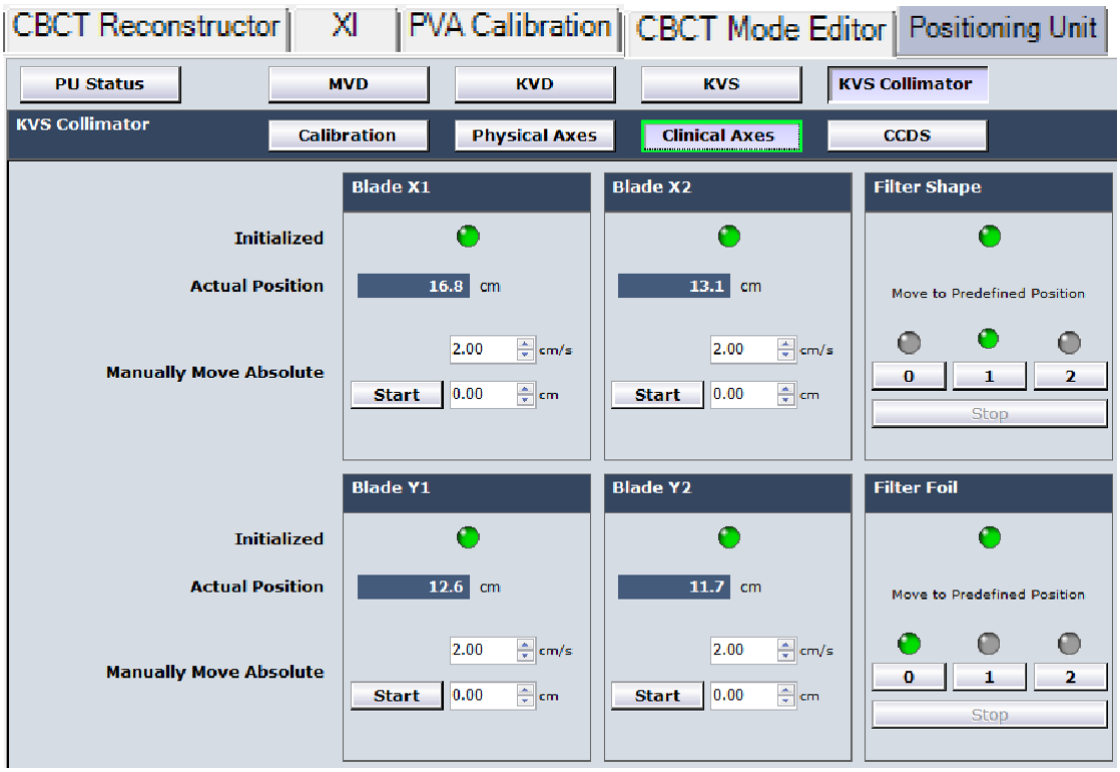

Figure 4.5: The "Positioning Unit" tab permitting manual movement of collimation and filtration axes. "Filter Shape" 0-2 correspond to: no bowtie, full-fan bowtie, half-fan bowtie respectively.

TrueBeam® operates based on instructions written in the extensible markup programming language (XML), which provides an ordered series of instructions to the machine. Given the correct instructions, the machine can be made to perform CBCT acquisition with tube voltages that are not available clinically. A generic XML script was written with functionality to perform continuous kV imaging with a gantry speed of 6° per second, at a frame rate of 15 frames per second, to give a total of 890 projections. The script was then modified to give a fixed tube current of 60 mA with a pulse length of 20 ms to give an equivalent exposure of 1.2 mAs per projection, for a total exposure of 1068 mAs. Various scripts were then saved after changing the tube potential parameter "<KiloVolts>" to: 40, 50, 60, 70, 90, 110, 120, and 130. The TrueBeam® Developer Mode platform was used to perform each acquisition with the same

phantoms and FOV as for the clinical acquisitions. To ensure that the collimation and filtration associated with clinical modes remained the same, collimator and bowtie filter positions were recorded, and then set in service mode before loading the XML script in Developer Mode.

4.4 Image processing

4.4.1 iTools reconstruction

The clinical CBCT Reconstructor® is limited to the calibration and acquisition data supplied from clinical CBCT modes. The iTools reconstruction software **[67]** developed by Varian™ gives researchers access to the same algorithms used by the clinical reconstructor to facilitate non-clinical reconstructions. Each reconstruction follows a procedure called the "reconstruction chain", which is a series of sequenced algorithms (plug-ins) that process the projection data until it is a reconstructed 3D image set.

The minimum processing steps required for all projections are:

1. Framework (read and extract raw data).
2. Log-normalization (by unattenuated air projection).
3. Filtering and decimation (apply corrections and data filter).
4. Backprojection.

Further steps include: HU mapping, ring suppression, analytic spectrum corrections (ASC), and scatter corrections (SC). See figure 4.6 for an image of the chain from iTools.

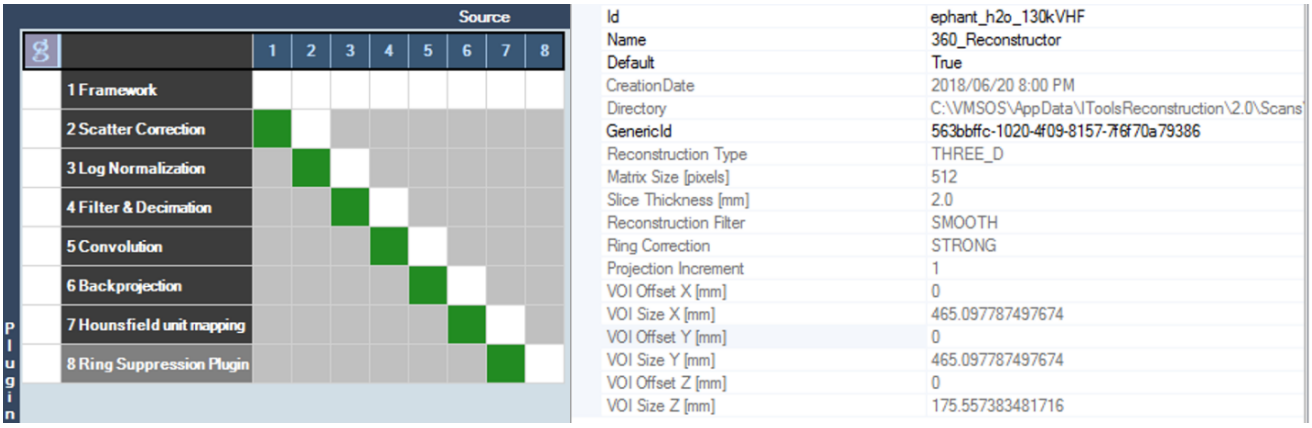

Figure 4.6: The reconstruction chain in iTools used for reconstruction of all Developer Mode acquisitions.

Before raw Developer Mode acquisitions were imported into iTools, the air norm calibrations were first performed by importing the raw projections with and without bowtie for each non-clinical tube potential that was used. Non-clinical CBCT modes were then created such that the correct air norm calibration would be applied upon loading in the phantom projections. As shown in figure 4.6, in addition to the minimum processing steps, SC, HU mapping and ring suppression were also applied. These extra corrections were applied in effort to make the reconstruction closer to a clinical reconstruction in which these corrections are applied. An issue arose upon trying to apply scatter corrections that were outside the clinically available range of tube potentials. Furthermore, the clinical ASC (beam hardening) only included attenuation data for clinical energies. Support was provided by Varian™ to acquire SC for all non-clinical tube potentials used in these experiments based on work by Sun and Star-Lack **[50]**, however an ASC for non-clinical energies was not used. This presented a limitation in comparison between clinical and non-clinical reconstructions; however non-clinical tube potential variation was deemed a feasible experiment, but results were not comparable to the clinical CBCT results.

4.4.2 Image quality analysis

CNR was defined as:

$$CNR = \frac{|\bar{S}_{ROI} - \bar{S}_B|}{\sigma_B} \tag{55}$$

Where S_{ROI} denotes the signal of a region of interest (ROI) in the image with contrast inserts, S_B is the average signal intensity in the background of the image with water inserts, and σ_B denotes the standard deviation of a ROI situated in the background of the image with water inserts.

To calculate CNR for these experiments, S_{ROI} was obtained by calculating the mean pixel value in a region of interest containing a contrast insert as illustrated in figure 4.7.

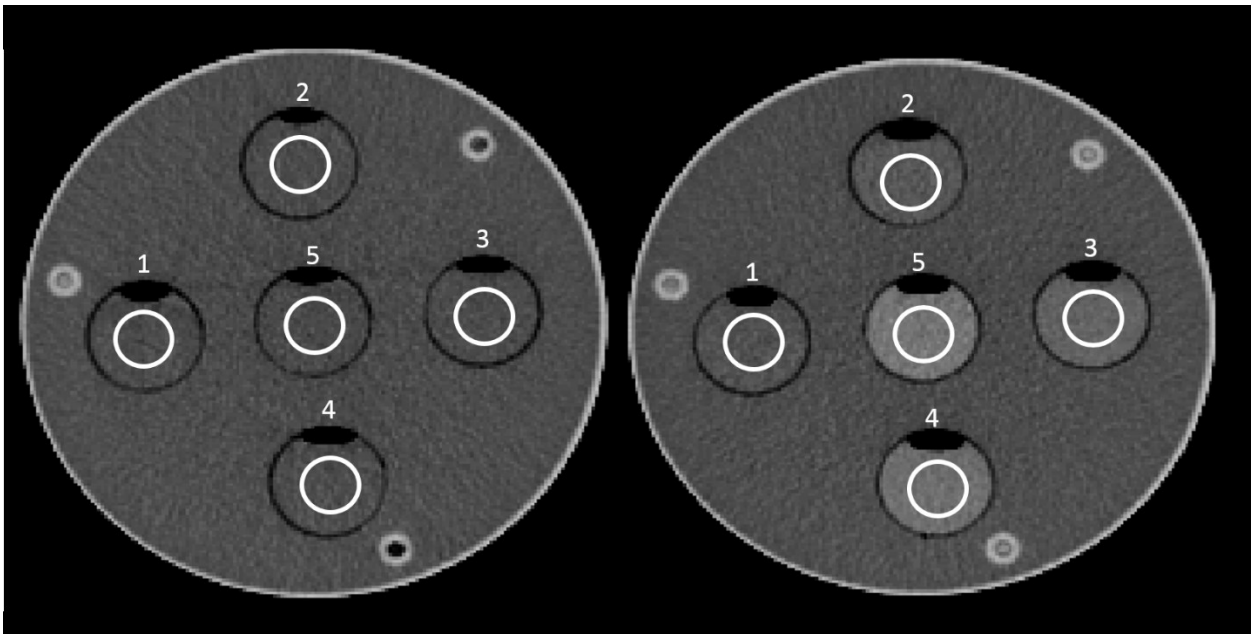

Figure 4.7: FBCT image for the cylindrical phantom demonstrating the ROI selected for CNR analysis, water inserts used for background signal and variance (left), and contrast inserts of concentrations: 0.0125 (1), 0.025 (2), 0.05 (3), 0.075 (4), 0.1 (5) mmol/kg (right) used for contrast signal.

S_B and σ_B were both acquired in the water-only image set to ensure that calculated CNR was not biased by any variations of uniformity across the FOV. CNR was calculated and averaged over ten slices in the phantom. Variability of CNR was quantified as the standard deviation across all slices. All analysis was performed using MATLAB (MathWorks, Natick, USA). CNR was deemed sufficient when above three, based on the Rose Criterion **[56]** for CNR. The same ROI were chosen for the CBCT images.

Chapter 5 Results

5.1 Imaging Gadoxetate Disodium with FBCT

As expected from the preclinical work performed of Schmitz *et al.* **[38]**, CNR was approximately linear with Gadoxetate Disodium concentration as demonstrated in figure 5.1. Fitting the data for the cylindrical phantom yielded slopes ranging from 46.5 $(mmol/kg)^{-1}$ for the 80 kVp tube potential, to 76.9 $(mmol/kg)^{-1}$ for the 140 kVp tube potential with Pearson Correlation coefficient ($R>0.99$) in all cases. In comparison, fitting the data for the ellipsoidal phantom yielded lower slope values ranging from 23.3 $(mmol/kg)^{-1}$ for the 80 kVp tube potential, and 35.9 $(mmol/kg)^{-1}$ for the 120 kVp tube potential ($R>0.98$).

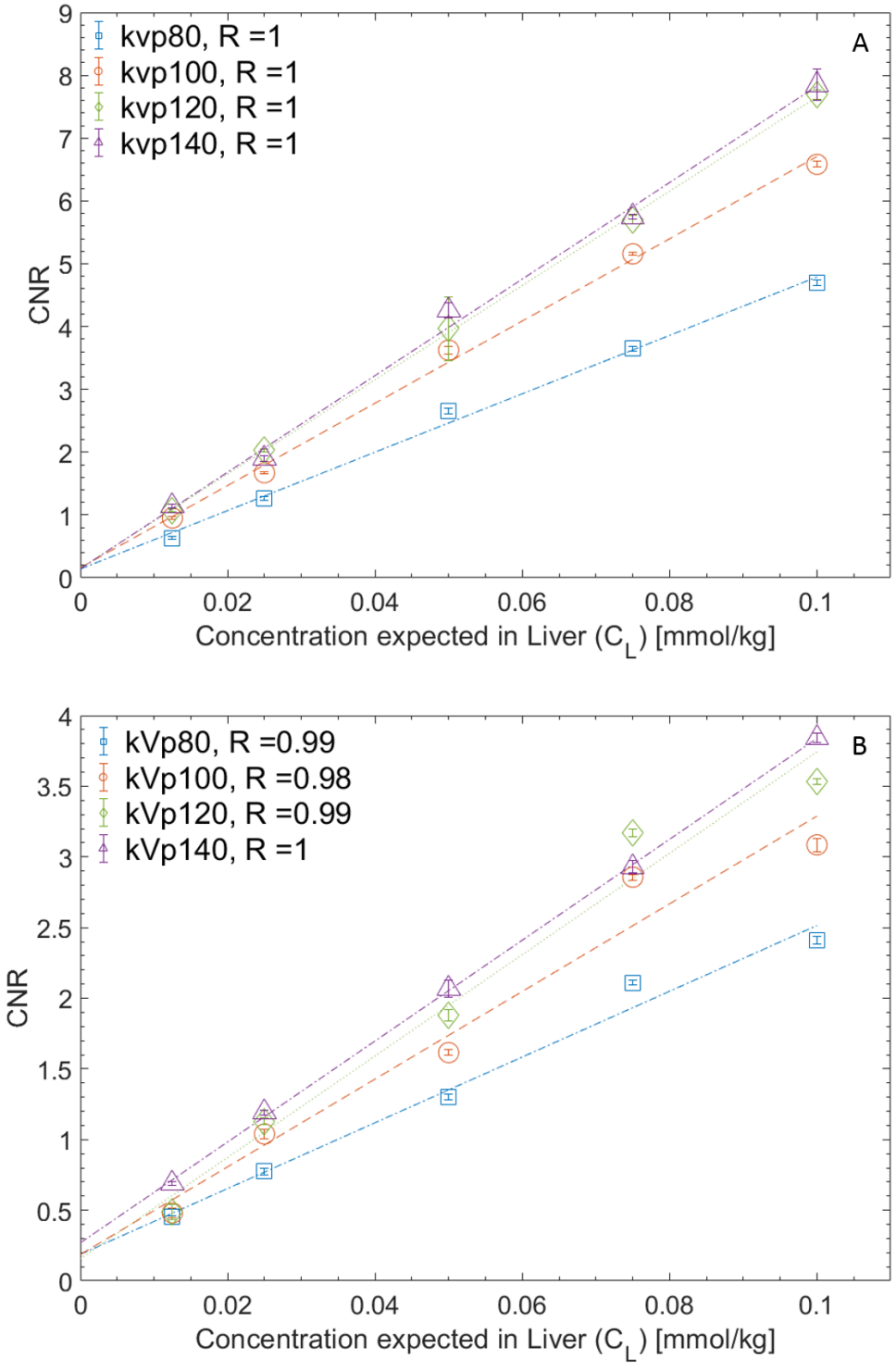

Figure 5.1: Image CNR as a function of concentration expected in the liver when imaging with FBCT for the cylindrical phantom ideal imaging geometry (A), and ellipsoidal phantom realistic abdomen geometry (B).

The results for the idealized cylindrical geometry in figure 5.1.A suggest that to achieve a sufficient CNR greater than three, a concentration in the liver of 0.05 mmol/kg or greater is required. Furthermore, with this concentration, FBCT imaging must be performed with a tube potential of 100 kVp or greater. Above 100 kVp we do not observe a substantial variation in CNR for concentrations less than 0.075 mmol/kg. At these concentrations, there was little variation in CNR between 120 and 140 kVp. The results for the ellipsoidal phantom (B) suggest that to achieve sufficient CNR greater than three, the liver must take up a concentration of 0.075 mmol/kg or greater. At a concentration of 0.1 mmol/kg there is no overlapping of data points. This could indicate that there is a greater dependence of CNR on tube potential as concentration increases in the ellipsoidal phantom.

5.2 Imaging Gadoxetate Disodium with CBCT

5.2.1 Clinical CBCT

Figure 5.2 demonstrates the results from CBCT performed on the cylindrical phantom for half-fan (HF, top), full-fan with half arc (FFHA, middle) and full-fan filtration with full arc (FFFA, bottom) acquisitions.

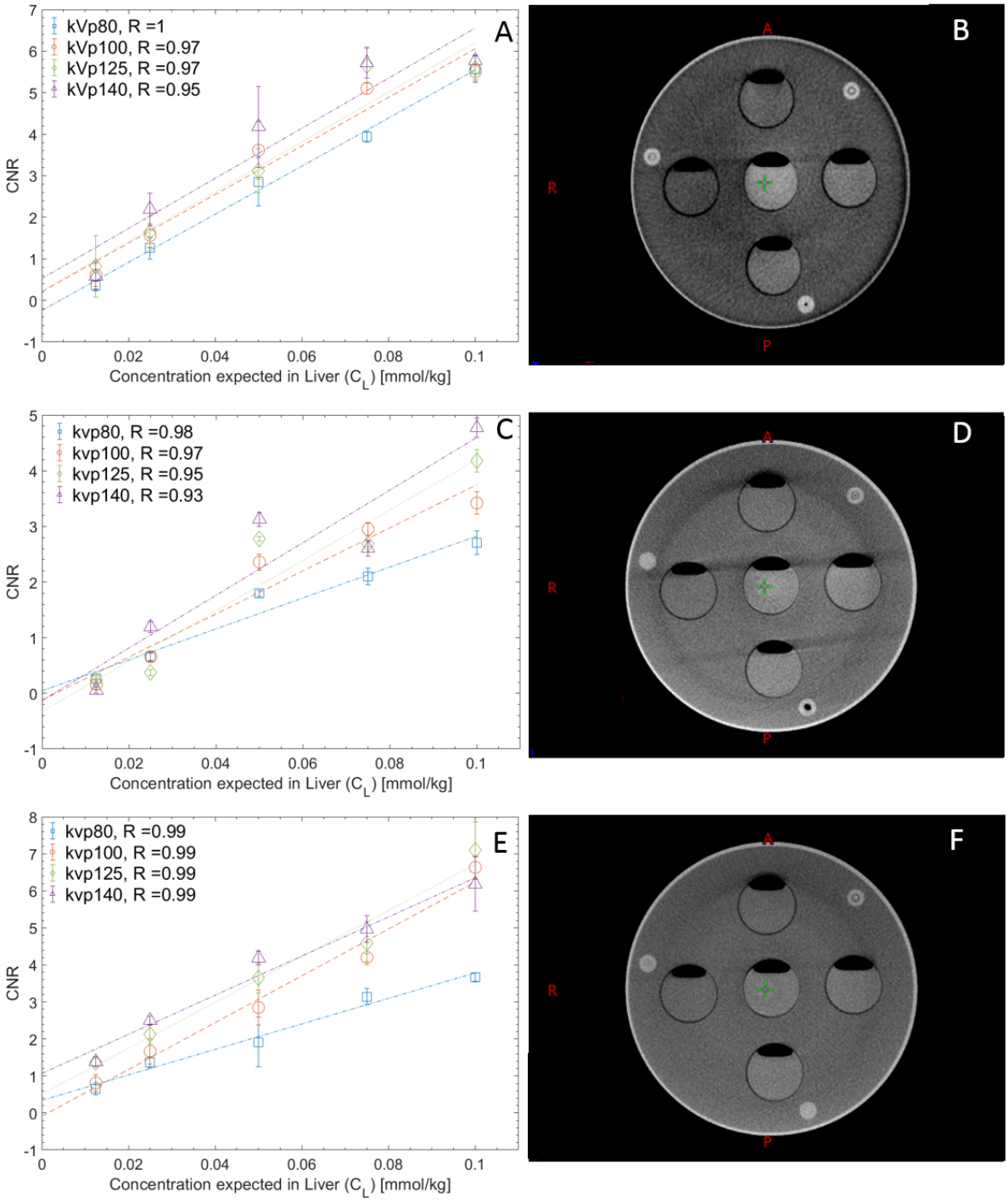

Figure 5.2: Image CNR as a function of concentration for the cylindrical phantom, with varying tube potentials and acquisition modes (left column). Representative axial slices are shown at 100 kVp to qualitatively demonstrate image quality (right). Acquisition modes are HF (A, B), FFHA (C, D), and FFFA (E, F).

The CBCT results for the geometry in figure 5.2 demonstrate that to achieve CNR greater than three, the liver must take up a concentration of 0.05 mmol/kg or greater. Viable tube potentials are those greater than 80 kVp in the HF acquisition, and greater than 125 kVp for the FFFA acquisition. The FFHA acquisition achieved CNR greater than three only for doses of 0.1 mmol/kg for tube potentials greater than 80 kVp. All acquisitions were fit linearly, to compare with the baseline data obtained in figure 5.1, and deviations from the fit were deemed to be caused by CBCT artifacts and non-uniformities in the measured data. The linear fits to the HF filtration data yielded slopes ranging from 57.9 $(mmol/kg)^{-1}$ for the 80 kVp tube potential to 60.3 $(mmol/kg)^{-1}$ for the 140 kVp tube potential. The linear fits on the FFHA data gave slopes ranging from 27.8 $(mmol/kg)^{-1}$ for the 80 kVp tube potential to 47.3 $(mmol/kg)^{-1}$ for the 140 kVp tube potential. Lastly, the linear fits on the FFFA data gave slopes ranging from 34.4 $(mmol/kg)^{-1}$ for the 80 kVp tube potential, to 63.3 $(mmol/kg)^{-1}$ for the 100 kVp tube potential ($R>0.93$).

For the ellipsoidal phantom, full-fan acquisitions truncated the phantom volume resulting in significant truncation artifacts that skewed the contrast in a similar manner to **[68]**. These were thus deemed unusable, and results from only half-fan acquisitions are shown in figure 5.3:

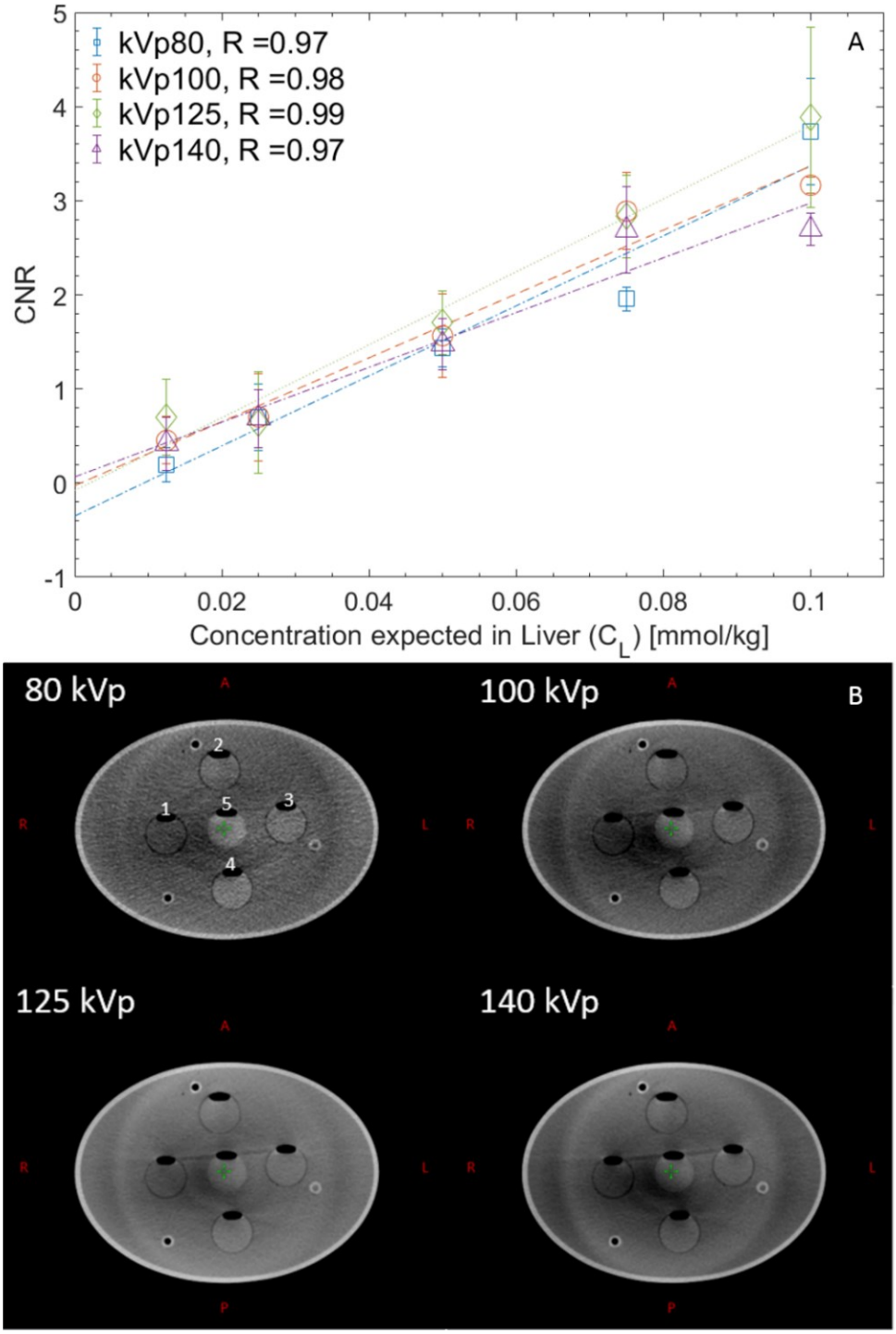

Figure 5.3: (A)Image CNR as a function of concentration expected in the liver for the ellipsoidal phantom, with varying tube potentials, constant exposure of 1080 mAs, and HF acquisition. (B) Axial slices taken from the treatment planning system (TPS) show typical artifacts, which were the dominant cause of CNR deviation from linearity.

The CBCT results from figure 5.3 demonstrate that to achieve a CNR greater than three, a minimum concentration in the liver of 0.1 mmol/kg is necessary, combined with a clinical tube potential of 80 kVp or greater. When fit linearly for comparison with figure 5.1, the slopes ranged from 29.1 $(mmol/kg)^{-1}$ at 140 kVp to 38.7 $(mmol/kg)^{-1}$ at 125 kVp.

CNR can be increased by using greater tube current or exposure time to improve noise characteristics **[47]**. To examine CNR improvement, exposure (mAs) was varied while maintaining the HF acquisition mode with 100 kVp; this is illustrated in figure 5.4. The choice for 100 kVp is further supported by the proximity of the average energy of this spectrum to the k-edge of Gd (50.2 keV).

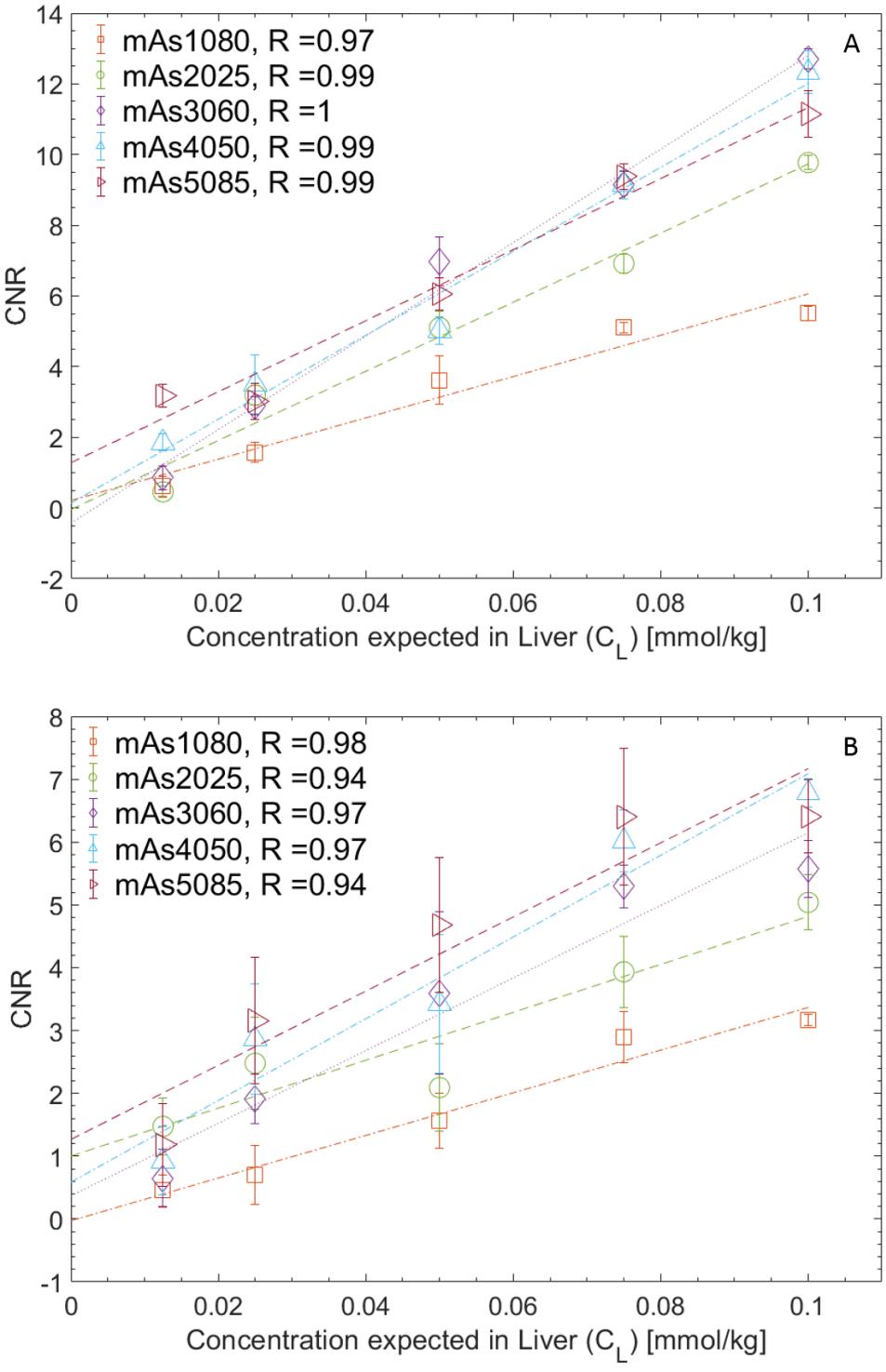

Figure 5.4: Image CNR as a function of concentration for various exposure settings, constant tube potential of 100 kVp and HF acquisition mode, for the cylindrical (A) and ellipsoidal (B) phantoms.

Figure 5.4.A demonstrates that to achieve adequate CNR above three, a concentration in the liver of 0.025 mmol/kg or greater is required for the exposure setting of 2025 mAs. Above 2025 mAs there is not substantial variation in CNR. For a concentration of 0.05 mmol/kg a tube current of 1080 mAs is required. For figure 5.4.B, the results demonstrate that to achieve an adequate CNR of three or greater, a liver concentration of 0.025 mmol/kg or greater is required. Given the variability of the data, an exposure as low as 4050 mAs may be possible at this dose.

5.2.2 Parameters to consider for a clinical trial

The results of this chapter have demonstrated various combinations of parameters that could be used in a clinical trial with Gadoxetate Disodium and CBCT. Table 5.1 summarizes the linear fitting results from figure 5.3A and 5.4B for the case of imaging the ellipsoidal phantom. An example calculation is as follows for the 80 kVp HF acquisition with an exposure of 1080 mAs:

$$CNR_{kVp,mAs} = k * C_L + CNR_0 \tag{56}$$

$$CNR_{Rose\ min} = 3$$

Equation 69 demonstrates the generic form of a linear fit to this data, where the minimum value of the Rose criterion can be substituted into the linear fit to solve for C_L:

$$CNR_{80kV,1080mAs} = 37.2\left[\frac{kg}{mmol}\right] * C_L\left[\frac{mmol}{kg}\right] - 0.3 \tag{57}$$

$$CNR_{Rose\ min} = 3$$

$$3 = 37.2\left[\frac{kg}{mmol}\right] * C_L\left[\frac{mmol}{kg}\right] - 0.3 \tag{58}$$

$$C_{L,min} = 0.0887 \left[\frac{mmol}{kg}\right]$$

Table 5.1: Summary table of CBCT imaging parameters kVp and mAs with associated minimum concentration in liver $C_{L,min}$ after administration of $C_{A,min}$ according to equations of fit for the ellipsoidal phantom

kVp	***mAs***	$C_{L,min}$ [mmol/kg BW]	$C_{A,min}$ [mmol/kg BW]	$C_{A,min}/C_{A,MRI}$
80	1080	0.0887	0.177	7
100	1080	0.0885	0.177	7
100	2025	0.0525	0.105	4
100	3060	0.0588	0.118	5
100	4050	0.0369	0.073	3
100	5085	0.0288	0.058	2
125	1080	0.0801	0.160	6
140	1080	0.0966	0.199	8

According to the equations of fit as well as the contrast derivation in chapter 4, to achieve adequate contrast enhancement in CBCT the Gadoxetate Disodium dosage regime must be increased relative to the current recommended dose. $C_{A,MRI}$ in the last column is the constant recommended dose of administration equal to 0.025 mmol/kg, these units will cancel with those of $C_{A,min}$ to give the administration multiplier.

5.2.3 Non-clinical CBCT

The results from this section provide a proof of concept for imaging Gadoxetate Disodium with CBCT modes using settings that are outside of the clinically available range, as well as a slightly different reconstruction chain than that used clinically. Figure 5.5 demonstrates example axial slices of the cylindrical phantom imaged with a tube potential of 60 kVp that has gone through the same calibration procedure as all clinical modes, except for applying a beam hardening correction.

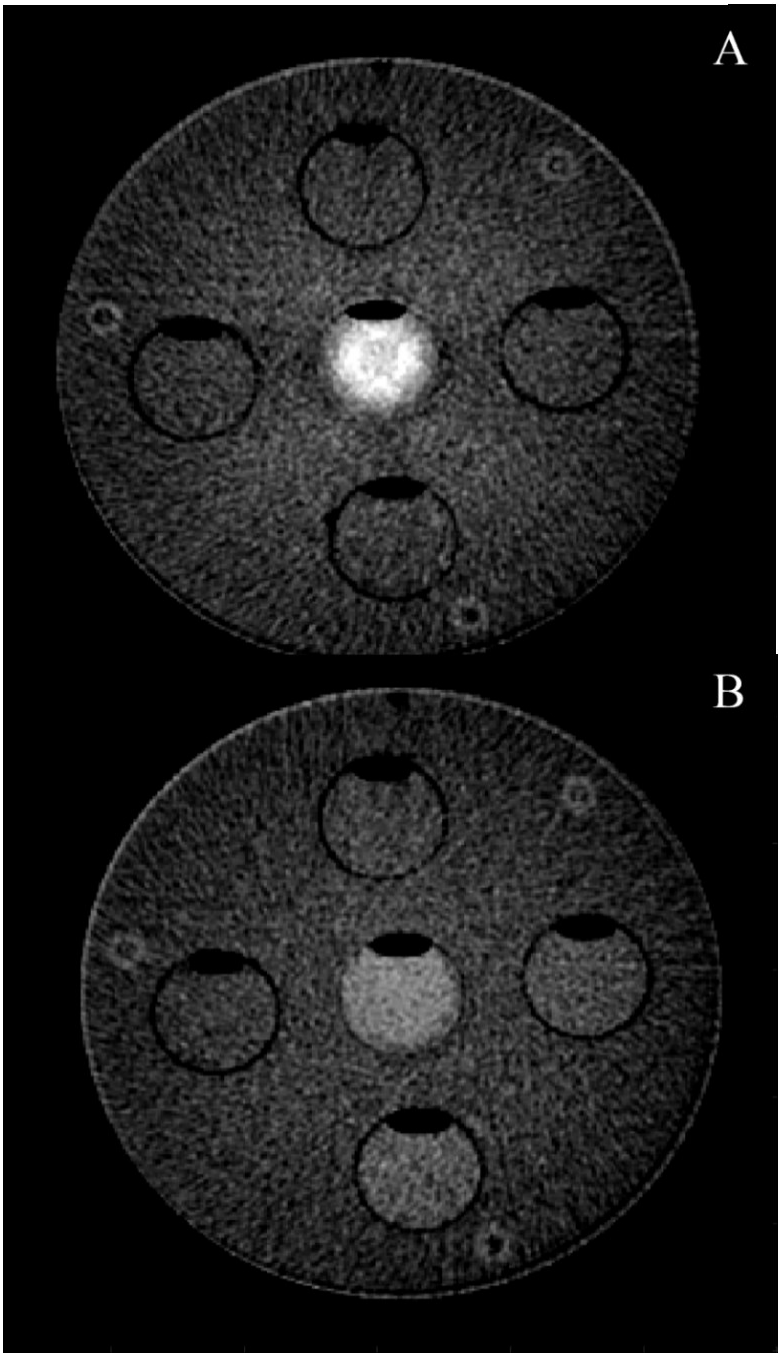

Figure 5.5: Axial slices of the cylindrical phantom with water inserts (A) and contrast inserts (B) with a CBCT acquired at 60 kVp with the same corrections applied as clinical mode except beam hardening. The images were window-leveled from -50 to 250 HU.

The water insert in the middle of figure 5.5A exhibited much higher attenuation than the other water inserts, and the contrast inserts. This could be a result of not applying the beam

hardening correction to the non-clinical reconstructions, and due to the increased photoelectric interactions, that occur in the phantom with contrast inserts the beam could have been softened compared to exclusively water inserts. This skewed results for the CNR calculation at 0.1 mmol/kg, corresponding to the insert at the center of the phantom. As this was a feasibility experiment to compare against the baseline CNR achieved from FBCT, the data for all non-clinical CBCT was fit linearly such that the CNR at 0.1 mmol/kg could be interpolated, instead of taking the measured value. The results are shown in figure 5.6:

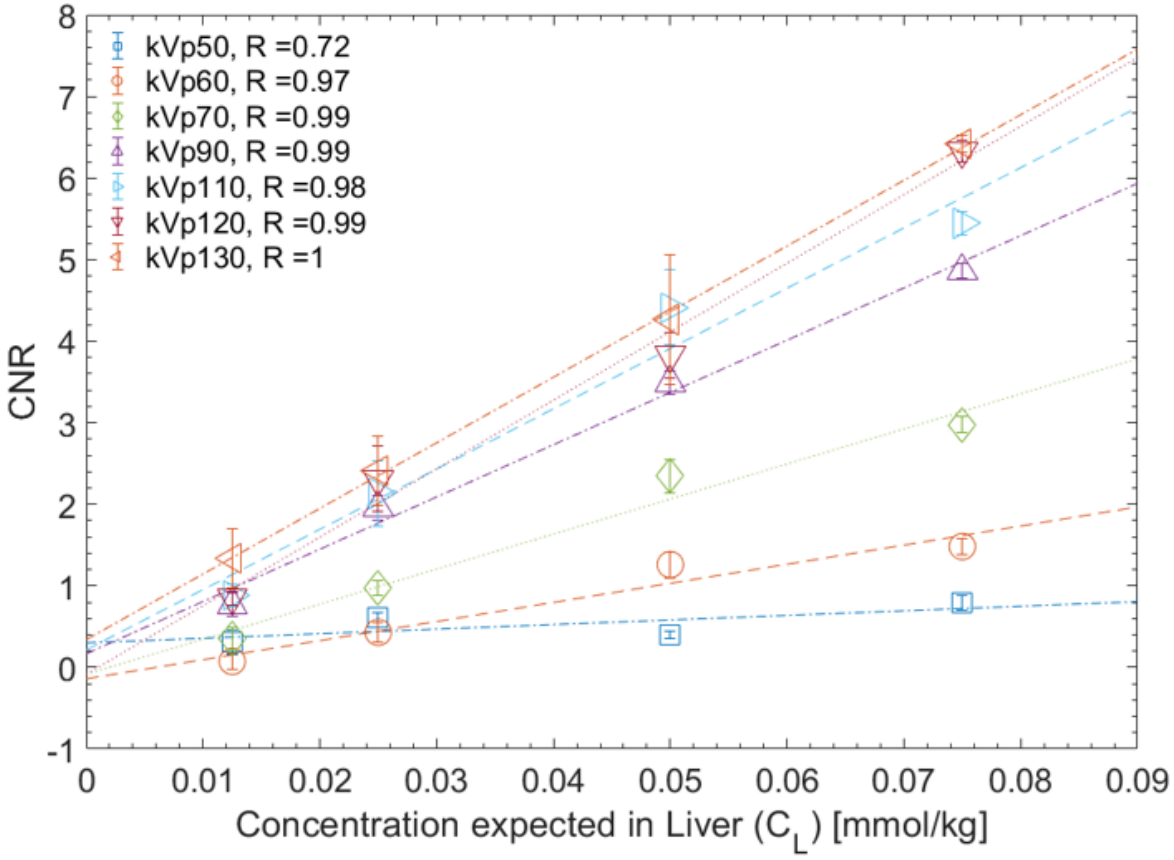

Figure 5.6: Illustrating image CNR as a function of concentration in the liver for various CBCT modes based on non-clinical tube voltages ranging from 50 – 130 kVp. Exposure was kept constant at 1068 mAs with a constant HF filtration, in the cylindrical phantom only

Figure 5.6 demonstrates that to achieve adequate CNR above three, a concentration in the liver of 0.05 mmol/kg or greater is required for the non-clinical tube voltage of 90 kVp. Above 90 kVp there is not considerable variation in CNR. This is evidenced by the clustering of data points at the concentration of 0.05 mmol/kg, above 90 kVp. When fit linearly for comparison with figure 5.1, the slopes ranged from 5.6 $(mmol/kg)^{-1}$ at 50 kVp to 84.0 $(mmol/kg)^{-1}$ at 120 kVp.

Chapter 6 Discussion

To our knowledge, this study is the first to perform analysis of FBCT and CBCT CNR with Gadoxetate Disodium (marketed as Primovist® in Canada and Europe, and Eovist® in the USA). The work was motivated by the findings of Schmitz *et al.* **[38, 39]** who performed a pre-clinical and a phase IIA clinical trial with Gadoxetate Disodium in 15 patients using helical FBCT in 1997. Because this study did not consider modern image quality metrics, it was deemed necessary to quantify CNR as a function of concentration. Given the liver specificity of the agent and appropriate time course of washout in the liver, this work has aimed to provide pre-clinical information dosing and imaging information that could address the limitations of iodinated contrast found by Eccles *et al.* **[30]** and Jones *et al.* **[29]**; specifically rapid clearance of the contrast agent from the liver. The data presented herein may inform clinical trials with Gadoxetate Disodium, with an aim toward improving image guidance during liver SBRT.

The recommended administration dose cited in the Primovist® product monograph **[33]** is 0.025 mmol/kg (body weight). The expected concentration in healthy liver cells is half of the administration dose **[33]** which would be 0.0125 mmol/kg (body weight) based on the recommendation. Any higher dose would be considered off-label use and at the discretion of the administering physician. Schmitz *et al.* **[39]** quoted administration doses of 0.2, 0.35, and 0.5 mmol/kg, which would correspond to expected liver concentrations of 0.1, 0.175, and 0.25 mmol/kg. Thomas *et al.* **[63]** quoted administration doses of 0.025 mmol/kg yielding insufficient image quality and received permission from the manufacturer to double the dose to 0.05 mmol/kg. This resulted in greater differences in attenuation between liver and lesions. According to the data given in our work, it should be feasible to achieve sufficient CNR given this administered dose with appropriate CBCT imaging protocols.

Figure 5.4 illustrates the effect of increasing exposure by increasing CBCT tube current output, for both geometries. In each case, the lower limit of the Rose criterion is met at a concentration lower than figures 5.2 and 5.3, implying that increasing exposure could permit lower doses to be administered. It is important to note that while giving sufficient CNR, some exposures are not clinically practical. For example, when starting with a cold x-ray tube (defined as 1 heating unit), 100 kVp and 5085 mAs will require tube cooling before the scan finishes. This would introduce unnecessary delays during the image guidance procedure. Given a cold x-ray tube, 100 kVp and 4050 mAs is feasible, however performing multiple of these scans could require undesirable wait times for tube cooling. Furthermore, if larger tube exposures are used, there could be greater skin doses as discussed in Islam *et al.* **[69]**.

At our centre, SBRT for the liver is normally delivered in five fractions, with image guidance being performed before every treatment. One issue concerns whether contrast may be delivered on each fraction. Clinical trials with this compound have not examined toxicities associated with repeated injections in humans **[33],** and therefore an unmet need exists for investigation. Furthermore, only a limited number of studies have examined the toxicities in humans associated with dose escalation with this contrast agent **[34]**. The major risk of using gadolinium-based contrast agents (GBCA) in MRI is the retention of Gadolinium, which has been associated with Nephrogenic Systemic Fibrosis (NSF) in patients with severely impaired renal function **[33]**. The product monograph describes two animal models used for repeated dosages: rats and dogs. Findings concluded that after 28 to 31 repeated doses (once per day), adverse effects were not observed in the minimum dose group in rats nor dogs of 0.2 and 0.1 mmol/kg, respectively [**70, 71]**.

While the concentrations to achieve acceptable CNR in CBCT imaging would correspond to dose values outside of the Primovist® dosing regimen, these results also agree qualitatively with the liver images provided by Schmitz *et al.* **[39]** and Thomas *et al.* **[63].** It is important to note that all experiments for this dissertation were performed with dilutions of the contrast agent, and the product monograph states that the molecule is soluble in water **[33]**. This implies that the molecule should dissociate, as compared to the expected binding that would occur when interacting with true hepatocytes. In our experiments we were measuring CNR with respect to a water background, whereas a clinical trial would be measuring CNR of a hypodense tumour with respect to the healthy liver background. It is the comparison relative enhancement that is important, and this supports CNR being the appropriate image quality metric to be applied for further translation of this research. Other image quality metrics related to the x-ray imaging system, such as detective quantum efficiency (DQE) and the modulation transfer function (MTF), are less appropriate for evaluating relative enhancement because they measure absolute performance of the system.

The feasibility study into non-clinical tube potentials was limited by the fact that the beam hardening correction that is applied to clinical projections was not available for non-clinical projections. This caused variability in the reconstruction chain and thus comparisons could not be reliably performed between clinical and non-clinical CBCT. However, the data obtained in figure 5.6 can be compared to the FBCT results of figure 5.1 in terms of the attainable CNR. As expected, increasing kVp increased CNR, likely due to improved DQE. Notably, image CNR was not plotted as a function of concentration for the ellipsoidal phantom due to significant artifacts. These artifacts were presumed to originate from scatter and beam hardening. Although a scatter dependent correction was obtained from Varian^{TM}, the results remained inconclusive.

Figure 5.6 proves the feasibility of performing CBCT with non-clinical modes in a geometry less likely to be hindered by scatter. This will become more important when considering future work, to be discussed in the next chapter.

Chapter 7 Conclusions

7.1 Summary of work

The purpose of this thesis, as outlined by the research objectives in chapter 1.5 was to perform a systematic quantification of CNR for Gadoxetate Disodium with CBCT. The original intention of this work was to provide an overview of parameter optimization, followed by a small clinical trial (N < 5), however the timeline for regulatory approval precluded starting the trial during the course of the research project. The results of this thesis first demonstrated baseline image quality for Gadoxetate Disodium enhanced helical FBCT. These results were then compared to similar methodologies published 20 years ago **[38, 39]**. The expectation was confirmed that with superior advances in technology, decreased amounts of contrast agent would be required, however these earlier studies did not perform CNR analysis which is an accepted medical image quality metric. CBCT imaging was first performed with an ideal imaging geometry to better understand the clinical imaging system's potential for use with this contrast agent, and the parameters tube potential, tube current, and filtration were investigated for image optimization. The results from these experiments confirmed expected trends with the baseline FBCT data and ensured confidence in the imaging system. CBCT imaging was then repeated, but with a more realistic ellipsoidal geometry to better represent a patient's abdomen. Physical theories of image quality decreasing with phantom size and imaging FOV were confirmed when maximum CBCT CNR was found to be higher for the cylindrical geometry. Nonetheless, acceptable image quality was quoted for the ellipsoidal phantom in table 5.1; illustrating that Gadoxetate Disodium can be visualized with CBCT, however, the recommended dose cannot be followed.

The results from this work combined with toxicities reported in **[33]**, and existing patient information from the late 1990s, warrant further scientific investigation of Gadoxetate Disodium in a radiotherapy setting. Moreover, this work has given a comprehensive analysis of the methodology required to assess feasibility of an intravenous contrast agent to be used for image guidance. With more focus on this area of research, it is reasonable to assume that invasive methods, such as having to surgically implanted markers into the liver or performing catheterized arterial injections, may be avoided.

7.2 Future work

7.2.1 Dual energy CBCT to acquire "Gadolinium" image

Dual energy (DE) imaging is a technique used in diagnostic imaging to remove anatomical noise from an image by acquiring the same image at both a low and high energy. By weighting the contributions of each image appropriately, this technique can effectively cancel contributions to a medical image from a specific material type **[47]**. For example, this is useful in soft-tissue imaging when there may be overlap of soft-tissue and bone, the low energy image should experience more photoelectric interactions with the higher Z bone, while the high energy image should experience more Compton scattering. Performing a specific DE subtraction will thus yield either a "bone only" image or "soft-tissue only" image.

Extending the DE technique to this research could have an advantage because of the high Z gadolinium atom that would enhance liver tissue. Moreover, the hepatocellular specific nature of the contrast agent implies that it should not be taken up by tumours **[33]**. If a DE subtraction is performed to acquire a "gadolinium only" image, the diseased liver that did not take up the

contrast agent should appear hypodense thus providing accurate information about its geographic location.

A comprehensive discussion on the theory behind dual energy imaging can be found in **[47]** however a pictorial example is given in figure 7.1.

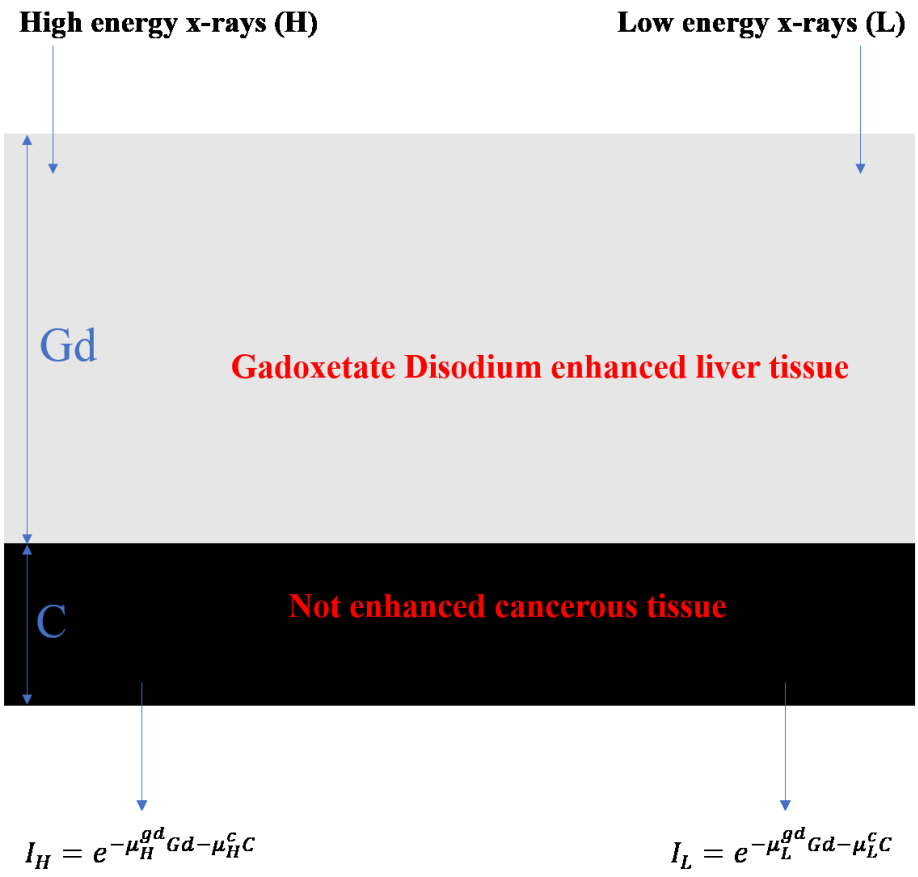

Figure 7.1: Illustration of the physics behind dual energy imaging for the hypothesized case of selecting between enhanced liver tissue and hypodense cancerous tissue.

Dual energy x-ray images are calculated from a logarithmic subtraction of two single energy images: one acquired from high energy (H) x-rays, and the other from low energy x-rays (L). The spectral energy dependence is reflected in the linear attenuation coefficients of the object's various materials. Considering figure 7.1, attenuation through the object is represented

by equations for both H and L images. The thicknesses: Gd, and C, denote the thicknesses of Gadoxetate Disodium enhanced liver, and cancerous tissue. Moreover, the attenuation coefficients $\mu_H^{gd}, \mu_L^{gd}, \mu_H^C, \; and \; \mu_L^C$ represent those for high energy x-rays interacting with the Gadoxetate Disodium enhanced liver, low energy x-rays interacting with Gadoxetate Disodium enhanced liver, high energy x-rays interacting with the cancerous tissue, and low energy x-rays interacting with cancerous tissue, respectively.

It can then be demonstrated that a "gadolinium only" image (Gd_{im}) can be achieved, or a "tumour only" image (C_{im}) according to the following equations attained by performing a log-subtraction on the high and low energy images.

$$Gd_{im} = \left[-\mu_H^{gd} + \frac{\mu_H^C}{\mu_L^C}\mu_L^{gd}\right] Gd \tag{59}$$

$$C_{im} = \left[\mu_H^C - \frac{\mu_H^{gd}}{\mu_L^{gd}}\mu_L^{gd}\right] C \tag{60}$$

If these images could be performed with adequate contrast at the time of SBRT for liver, there would be much more reliability for matching, which may lead to the possibility for decreasing treatment margins, thereby introducing an opportunity for dose escalation to the tumour or improved organ-at-risk sparing.

Zbijewski *et al*. **[72]** demonstrated a dual-filtration technique with CBCT and observed the effect on a reconstruction algorithm's ability to classify materials. Low energy images were acquired with a 0.2 mm thick copper filter, whereas high energy images were acquired after

being filtered by 0.2 mm of copper and 0.5 mm of silver. There is a single titanium filtration option on TrueBeam® which was used for all varying kVp acquisitions. If differential filtration could be applied similar to **[72],** the gadolinium images could be further improved.

One main issue with performing dual energy imaging with the current kV system on TrueBeam® is the limitation of only four tube spectra. The preliminary results of figure 5.6 demonstrate that CBCT can be taken over a wider range of tube spectra, and thus dual energy implementation becomes a post-processing problem.

7.2.2 Monte Carlo measurements of skin dose

The CBCT protocols proposed in this research concern significant tube exposures on the order of those used for helical FBCT abdominal imaging. Instead of relying on surrogate dose measuring devices such as film, MOSFET, or OSLD **[47]**, Monte Carlo techniques can be used to simulate and estimate dose to skin.

A comprehensive discussion on Monte Carlo modelling of radiation transport can be found in **[73]**. It will suffice to briefly describe Monte Carlo in this context as a set of methodologies that model photon transport equations (interaction cross sections) probabilistically, thus using random numbers to predict radiation transport.

The electron gamma shower Monte Carlo simulation tool of the National Research Council (EGSNRC), can be used to import a patient CT set and then simulate radiation transport to that dataset. The BEAMnrc package can be used to design a kV x-ray tube with exact specifications provided by Varian™. Using this information, any set of imaging parameters can be evaluated, while simultaneously being able to calculate the exact skin dose from those imaging parameters.

7.2.3 Clinical trial with Gadoxetate Disodium and CBCT for SBRT

After consulting Health Canada at the beginning of this research, they deemed that there was not enough pre-clinical information at the doses proposed to justify performing a small phase IV clinical trial. The drug at the proposed dose was required to be submitted to Health Canada as a new drug and undergo regulatory approval. The original dose proposed in the ethics submission was an administration (C_A) of 0.1 mmol/kg. This dose was assumed safe because it is equivalent to the dose administered for various other GBCA in MRI, furthermore clinical trials with Gadoxetate Disodium investigated this dose extensively with an acceptably low probability of drug related adverse reactions **[33**]. Considering C_A equal to 0.1 mmol/kg, this corresponds to the C_L quoted on all results of 0.05 mmol/kg. The results of table 5.1 demonstrate that although improved contrast is found for higher doses, this dose may be feasible given the appropriate imaging parameters.

In addition, the issue of repeated injections, e.g., over a five-fraction regimen, is important to consider, as the clinical trial should not involve changes to the treatment routine except for introducing the contrast agent. Justification must be given for giving five contrast injections every second day. This timeline agrees with the washout of Gadoxetate Disodium in a patient with normal renal function given the elimination half-life quoted in the product monograph **[33]**.

Bibliography

[1] Canadian Cancer Statistics, *2017 Special Topic: Pancreatic cancer*, Canada (2017). Retrieved from:http://www.cancer.ca/~/media/cancer.ca/CW/cancer%20information/cancer%20101/Canadian%20cancer%20statistics/Canadian-Cancer-Statistics-2017-EN.pdf

[2] World Health Organization, *Cancer Fact sheets*, Switzerland (2018). Retrieved from: http://www.who.int/en/news-room/fact-sheets/detail/cancer

[3] S. Manfredi, C. Lepage, C. Hatem, O. Coatmeur, J. Faivre, and A.M. Bouvier. "Epidemiology and Management of Liver Metastases From Colorectal Cancer", Ann Surg, **244**(2). 254-259. (2006).

[4] M. Scorsetti, E Clerici, and T. Comito. "Stereotactic body radiation therapy for liver metastases," J Gastrointest Oncol, **5**(3). 190-197. (2014).

[5] E.J. Hall and A.J. Giaccia, *Radiobiology for the Radiologist,* 7th ed. (Wolters Kluwer Health/Lippincott Williams & Wilkins, Philadelphia, PA, 2012).

[6] E.B. Podgorsak, *Radiation Physics for Medical Physicists* (Springer, 2006).

[7] Canadian Cancer Statistics, *2013 Special Topic: Liver Cancer*, Canada (2013). Retrieved from: http://www.cancer.ca/~/media/cancer.ca/CW/cancer%20information/cancer%20101/Canadian%20cancer%20statistics/canadian-cancer-statistics-2013-EN.pdf?la=en

[8] J.R. Kallini, A. Gabr, R. Salem, and R.J. Lewandowski. "Transarterial Radioembolization with Yttrium-90 for the Treatment of Hepatocellular Carcinoma," Adv Ther, 33. 699-714. (2016).

[9] C.J. Karzmark, C.S. Nunan, and E. Tanabe, *Medical Electron Accelerators* (McGraw-Hill, INC. Health Professions Division, 1993)

[10] A. Brahame. “Multi leaf collimator,” US4672212A. (1985). Retrieved from: https://patents.google.com/patent/US4672212A/en

[11] K. Otto. “Volumetric Modulated arc therapy: IMRT in a single gantry arc,” Med Phys, **35**(1). 310-317. (2008).

[12] Y. Nagata. *Stereotactic Body Radiation Therapy: Principles and Practices*. (Springer Japan, 2015).

[13] L. Leksell. “The stereotaxic method and radiosurgery of the brain,” Acta Chirurgica Scandinavica, **102**(4). 316-319. (1951).

[14] W. Park, D.H. Lim, S.W. Paik, K.C. Koh, M.S. Choi, C.K. Park, B.C Yoo, J.E. Lee, M.K Kang, Y.J. Park, H.R. Nam, Y.C. Ahn, and S.J. Huh. “Local radiotherapy for patients with unresectable hepatocellular carcinoma,” Int J Radiat Oncol Biol Phys, **61**(4). 1143:1150. (2005).

[15] M.T. Lee, J.J. Kim, R. Dinniwell, J. Brierley, G. Lockwood, R. Wong, B. Cummings, J. Ringash, R.V. Tse, J.J. Knox, and L.A. Dawson. “Phase I study of individualized stereotactic body radiotherapy of liver metastases,” J Clin Oncol, **27**(10). 1585-1591. (2009).

[16] T.E. Schefter, B.D. Kavanagh, R.D. Timmerman, H.R. Cardenes, A. Baron, and L.E. Gaspar. “A phase I trial of stereotactic body radiation therapy (SBRT) for liver metastases,” Int J Radiat Oncol Biol Phys, **62**(5). 1371-1378. (2005).

[17] C.C. Pan, B.D. Kavanagh, L.A. Dawson, X.A. Li, S.K. Das, M. Miften, and R.K. Ten Haken. “Radiation-Associated Liver Injury,” Int J Radiat Oncol Biol Phys, **76**(30). S94-100. (2010).

[18] S.B. Kaginelli, T. Rajeshwari, Sharanabasappa, B. R. Kerur, and A.S. Kumar. “Effective atomic numbers and electron density of dosimetric material,” J Med Phys, **34**(3). 176-179. (2009).

[19] L. Xing, J. Chang, and C.G. Orton. “Point/Counterpoint: Kilovoltage imaging is more suitable than megavoltage imaging for guiding radiation therapy”, Med Phys, **34**(12). (2007).

[20] R.L. Siddon. “Fast calculation of the exact radiological path for a three-dimensional CT array,” Med Phys, **12**(2), 252-255 (1985).

[21] L. Feldkamp, L. Davis, and J. Kress, “Practical cone-beam algorithm,” JOSA A, **1**(6). 612-619. (1984).

[22] E.E. Klein, J. Hanley, J. Bayouth, F.F. Yin, W. Simon, S. Dresser, C. Serago, F. Aguirre, L. Ma, B. Arjomandy, and C. Liu. “Task Group 142 report: Quality assurance of medical accelerators”. Med Phys, **36**(9). 4197-4212. (2009).

[23] R.L. Baron. “Understanding and optimizing use of contrast material for CT of the liver,” AJR, **163**(2). 323-331. (1994).

[24] W. Wunderink, A. Mendez Romero, Y. Seppenwoolde, H. de Boer, P. Levendag, and B. Jeijmen. “Potentials and Limitations of Guiding Liver Stereotactic Body Radiation Therapy Set-Up on Liver Implanted Fiducial Markers,” Int J Radiat Oncol Biol Phys, **77**(5). 1573-1583. (2010).

[25] G. Oldrini, H. Taste-George, S. Renard-Oldrini, A.S. Baumann, V. Marchesi, P. Troufleau, D. Peiffert, A. Didot-Moisei, B. Boyer, B. Grignon, and P. Henrot. “Implantation of fiducial markers in the liver for stereotactic body radiation therapy: Feasibility and results,” Diag Interv Imag, **96**(6). 589-592, (2015).

[26] K. Kitamura, H. Shirato, S. Shimizu, N. Shinohara, T. Harabayashi, T. Shimizu, Y. Kodama, H. Endo, R. Onimaru, S. Nishioka, H. Aoyama, K. Tsuchiya, and K. Miyasaka. “Registration accuracy and possible migration of internal fiducial gold marker implanted in prostate and liver treated with real-time tumor-tracking radiation therapy (RTRT),” Radiother Oncol, **62**(3):275-281. (2002).

[27] Y. Seppenwoolde, W. Wunderink, S.R. Wunderink-van Veen, P. Storchi, A. Mendez Romero, and B.J. Heijmen. “Treatment precision of image-guided liver SBRT using implanted fiducial markers depends on marker-tumour distance,” Phys Med Biol, **56**(17). 5445-5468. (2011).

[28] MRIequip. *Gold Fiducial Markers. Our Products: MRI Imaging Aids > Markers. SKU: BP-107X.* Retrieved from: http://www.mriequip.com/store/pc/viewPrd.asp?idproduct=1468

[29] Radiology Info. *Fiducial Marker Placement*. Retrieved from: https://www.radiologyinfo.org/en/info.cfm?pg=fiducial-marker

[30] B.L. Jones, C. Altunbas, B. Kavanagh, T. Schefter, and M. Miften. "Optimized dynamic contrast-enhanced cone-beam CT for target visualization during liver SBRT," Int J Radiat Oncol Biol Phys, **489**(012035). (2014).

[31] C.L. Eccles, R.V. Tse, M.A Hawkins, M.T. Lee, D.J. Moseley, and L.A. Dawson. "Intravenous contrast-enhanced cone beam computed tomography (IVCBCT) of intrahepatic tumors and vessels," Adv Radiat Oncol, **1**(1). 43-50. (2016).

[32] G. Schuhmann-Giampieri, M. Mahler, G. Roll, R. Maibauer, and S. Schmitz. "Pharmacokinetics of the liver specific contrast agent Gd-EOB-DTPA in relation to contrast-enhanced liver imaging in humans," J Clin Pharmacol, **37**(7). 587-596. (1997).

[33] Bayer Inc. *Product Monograph Primovist*®. Mississauga, Ontario. (2017).

[34] B. Hamm, T. Staks, A. Muhler, M. Bollow, M. Taupitz, T. Frenzel, K.J. Wolf, H.J. Weinmann, and L. Lange. "Phase I clinical evaluation of Gd-EOB-DTPA as a hepatobiliary MR contrast agent: safety, pharmacokinetics, and MR imaging," Radiology, **195**(3). 785-792. (1995).

[35] P. Reimer, E.J. Rummeny, K. Shamsi, T. Balzer, H.E. Daldrup, B. Tombach, T. Hesse, T. Berns, and P.E. Peters. "Phase II clinical evaluation of Gd-EOB-DTPA: dose, safety aspects, and pulse sequence," Radiology, **199**(1). 177-183. (1996).

[36] D.A. Bluemke, D. Sahani, M. Amendola, T. Balzer, J. Breuer, J.J. Brown, D.D. Casalino, P.L. Davis, I.R. Francis, G. Krinsky, F.T. Lee, D. Lu, E.K. Paulson, L.H. Schwartz, and E.S. Siegelman. "Efficacy and safety of MR imaging with liver-specific contrast agent: U.S. multicenter phase III study," Radiology, **237**(1). 89-98. (2005).

[37] J. Endrikat, S.Y. Kim, T. Sakaguchi, S. Dohanish, and J. Breuer. "Safety of gadoxetate disodium: results from six clinical phase IV studies in 8194 patients," Acta Radiol, **57**(11). 1326-1333. (2016).

[38] S.A. Schmitz, S. Wagner, G. Schuhmann-Giampieri, W. Krause, and K.J. Wolf. "A prototype liver-specific contrast medium for CT: Preclinical evaluation of gadoxetic acid disodium, or Gd-EOB-DTPA," Radiology, **202**(2). 407-412. (1997).

[39] S.A. Schmitz, J.H. Haberle, T. Balzer, K. Shamsi, J. Boese-Landgraf, and K.J. Wolf. "Detection of focal liver lesions: CT of the hepatobiliary system with gadoxetic acid disodium, or Gd-EOB-DTPA," Radiology, **202**(2). 399-405. (1997).

[40] F. H. Attix. *Introduction to Radiological Physics and Radiation Dosimetry*. (Wiley, 1986).

[41] A.W. Wood, and K. Karipidis. *Non-ionizing Radiation Protection: Summary of Research and Policy Options.* (John Wiley & Sons, 2017).

[42] C. Grupen. *Introduction to Radiation Protection: Practical Knowledge for Handling Radioactive Sources.* (Springer, 2010).

[43] International Commission of Radiation Units and Measurements. *Tissue substitutes in radiation dosimetry and measurement ICRU Report 44*. (International Commission on Radiation Units and Measurements, Bethesda, MD, 1989).

[44] J.H. Hubbell and S.M. Seltzer. *Report No NISTIR 5632: Tables of x-ray mass attenuation coefficients and mass energy-absorption coefficients 1 keV to 20 MeV for elements Z=1 to 92 and 48 additional substances of dosimetric interest.* (National Institute of Standards and Technology, Gaithersburg, MD, 1995).

[45] J.E. Turner. *Atoms, Radiation, and Radiation Protection.* 3rd ed. (Wiley, 2007).

[46] M.J. Berger and S.M. Seltzer. *Stopping Powers and Ranges of Electrons and Positrons (2nd Ed.).* (National Bureau of Standards, Washington, DC, 1983).

[47] J.T. Bushberg, J.A. Seibert, E.M. Leidholt, and J.M. Boone. *The Essential Physics of Medical Imaging*, 3rd ed. (Lippincott Williams & Wilkins, Philadelphia, PA, 2011).

[48] K.K. Brock. *Image Processing in Radiation Therapy.* (CRC Press, 2014).

[49] D.L. Parker. "Optimal short scan convolution reconstruction for fanbeam CT," Med Phys, **9**(2). 254-257. (1982).

[50] M. Sun and J.M. Star-Lack. "Improved scatter correction using adaptive scatter kernel superposition," Phys Med Biol, **55**. 6695-6720. (2010).

[51] J. Star-Lack, M. Sun, A. Kaestner, R. Hassanein, G. Virshup, T. Berkus, and M. Oelhafen. "Efficient scatter correction using asymmetric kernels," Proc of SPIE, **7258**(72581Z-1). (2009).

[52] J. Star-Lack, J. Starman, P. Munro, A. Jeung, J. Richters, H. Mostafavi, and J. Pakovich. "A fast variable-intensity ring suppression algorithm," Med Phys, **33**(6). (1997).

[53] H. Turbell. *Cone-Beam Reconstruction Using Filtered Backprojection*. (Linkoping Studies in Science and Technology Dissertation No. 672, 2001).

[54] H. Yu, S. Zhao, and G. Wang. "A differentiable Shepp-Logan phantom and its applications in exact cone-beam CT," Phys Med Biol, **50**(23). 5583. (2005).

[55] J.H. Siewerdsen and D.A. Jaffray. "Cone-beam computed tomography tomography with a flat panel imager: Magnitude and effects of x-ray scatter," Med Phys **28**(2). 220-231. (2001).

[56] A. Rose. *Vision: Human and electronic.* (Plenum Press, 1973).

[57] A.E. Burgess. "The Rose model, revisited," J Opt Soc Am A, **16**(3). 633-646. (1999).

[58] H. Lusic and M.W. Grinstaff. "X-Ray Computed Tomography Contrast Agents," Chem Rev, **113**. 1641-1666. (2013).

[59] W. Giles, J. Bowsher, H. Li, and F.F. Yin. “Crescent artifacts in cone-beam CT,” Med Phys, **38**(4). 2116-2121. (2011).

[60] R.C. Orth, J.M. Wallace, M.D. Kuo, and Technology Assessment Committee of the Society of Interventional Radiology. “C-arm cone-beam CT: general principles and technical considerations for use in interventional radiology,” J Vasc Interv Radiol, **19**(6). 814-820. (2008).

[61] K. Suzuki, M.L. Epstein, R. Kohlbrenner, S. Garg, A. Oto, and R.L. Baron. “Quantitative radiology: automated CT liver volumetry compared with interactive volumetry and manual volumetry,” AJR Am J Roentgenol, **197**(4). W706-712. (2011).

[62] D. Parsons, and J.L. Robar. “An investigation of kV CBCT image quality and dose reduction for volume-of-interest imaging using dynamic collimation,” Med Phys **42**(9). 5258-5269. (2015).

[63] J.V. Thomas, D.N. Bolus, B.E. Jackson, L.L. Berland, M. Yester, and D.E. Morgan. “Gadoxetate disodium enhanced spectral dual-energy CT for evaluation of cholangiocarcinoma: Preliminary data,” Ann Med Surg (Lond), **6**. 17-22. (2016).

[64] D.A. Jaffray and J.H. Siewerdsen. “cone-beam computed tomography with a flat panel imager: Initial performance characterization,” Med Phys, **27**(6). 1311-1323. (2000).

[65] Varian Medical Systems Inc. *TrueBeam technical reference guide – Volume 2: Imaging.* (Varian Medical Systems Inc., 2016).

[66] Varian Medical Systems Inc. Service Engineer. (2018, May). Personal interview.

[67] Varian Medical Systems Inc. *User Manual: iTools – Reconstruction*. 2nd edition. (Varian Medical Systems Inc., 2013).

[68] S.H. Manglos. “Truncation artifact suppression in cone-beam radionuclide transmission CT using maximum likelihood techniques: evaluation with human subjects,” Phys Med Biol, **37**. 549. (1992).

[69] M.K. Islam, T.G. Purdie, B.D. Norrlinger, H. Alasti, D.J. Moseley, M.B. Sharpe, J.H. Siewerdsen, and D.A. Jaffray. “Patient dose from kilovoltage cone beam computed tomography imaging in radiation therapy,” Med Phys, **33**(6). 1573-1582. (2006).

[70] N. Kato, T. Yokawa, A. Tamura, A. Heshiki, W. Ebert, and H.J. Weinmann. “Gadolinium ethoxybenzyl-diethylenetriamine-pentaacetic acid interaction with clinical drugs in rats,” Invest Radiol, **37**(12). 680-684. (2002).

[71] S.A. Schmitz, S. Wagner, G. Schuhmann-Giampieri, W. Krause, M. Bollow, and K.J. Wolf. “Gd-EOB-DTPA and Yb-EOB-DTPA: Two prototypic contrast media for CT detection of liver lesions in dogs,” Radiology, **205**(2). 261-366. (1997).

[72] W. Zbijewski, G.J. Gang, J. Xu, A.S. Wang, J.W. Stayman, K. Taguchi, J.A. Carrino, and J.H. Siewerdsen. “Dual-energy cone-beam CT with a flat-panel detector: Effect of reconstruction algorithm on material classification,” Med Phys, **41**(2). 2-15. (2014).

[73] I. Kawrakow, E. Mainegra-Hing, D.W.O. Rogers, F. Tessier, and B.R.B. Walters. *The EGSnrc Code System: Monte Carlo Simulation of Electron and Photon Transport*. NRCC Report PIRS-701. (Ionizing Radiation Standards, National Research Council Canada, Ottawa, Canada, 2017).